J. Fluid Mech. (1992), *vol.* 238, *pp.* 537–577
Printed in Great Britain

The three-dimensional stability of boundary-layer flow over compliant walls

By K. S. YEO

Department of Mechanical and Production Engineering, National University of Singapore, 10 Kent Ridge Crescent, Singapore 0511, Republic of Singapore

(Received 8 February 1991)

This paper examines the linear stability of the Blasius boundary layer over compliant walls to three-dimensional (oblique) disturbance wave modes. The formulation of the eigenvalue problem is applicable to compliant walls possessing general material anisotropy. Isotropic-material walls and selected classes of anisotropic-material walls are studied. When the properties of the wall are identical with respect to all oblique wave directions, the stability eigenvalue problem for unstable three-dimensional wave modes may be reduced to an equivalent problem for two-dimensional modes. The results for isotropic-material walls show that three-dimensional Tollmien–Schlichting instability modes are more dominant than their two-dimensional counterparts when the walls are sufficiently compliant. The critical Reynolds number for Tollmien–Schlichting instability may be given by three-dimensional modes. Furthermore, for highly compliant walls, calculations based solely on two-dimensional modes are likely to underestimate the maximum disturbance growth factor needed for transition prediction and correlation. However, because the disturbance growth rates on highly compliant walls are much lower than those on a rigid wall, significant delay of transition may still be possible provided compliance-induced instabilities are properly suppressed. Walls featuring material anisotropy which have reduced stiffness to shear deformation in the transverse and oblique planes are also investigated. Such anisotropy is found to be effective in reducing the growth rates of the three-dimensional modes relative to those of the two-dimensional modes.

1. Introduction

The stability of boundary-layer flow over compliant surfaces has received considerable attention in recent years. This interest has been motivated to a large extent by the potential application of compliant surfaces as transition-delaying devices, and by related applications in the area of flow-noise control. The concept of boundary-layer stabilization through the use of compliant surfaces has generally been attributed to M. O. Kramer, who carried out, in the late 1950s, a series of experiments on streamlined bodies covered with a specially designed compliant coating. Kramer (1960) reported that the use of his compliant coating resulted in drag reductions of up to 60% over equivalent rigid models. Kramer in turn had derived his idea from the pioneering work of Gray (1936) on dolphins. In his study of the physiology of the dolphin, Gray, a biologist, found (based on the knowledge of his time) that he could not explain the exceptional swimming speeds of the dolphin unless he postulated a laminar boundary layer over the animal although turbulent flow was to be expected. This led Gray to believe that the dolphin probably possesses

the ability to stabilize the boundary layer over its body. The compliant coating designed and studied by Kramer in the late 1950s in fact represented his attempt to simulate the operation of the dolphin's epidermis in keeping the boundary layer over its body laminar. For a streamlined body, the maintenance of laminar flow is highly desirable, not only for its low skin friction but also for its very low noise. A brief historical survey of the subject may be found in Yeo (1986).

The earliest compliant wall model to be studied theoretically is the tensioned membrane; see Benjamin (1960, 1963), Landahl (1962) and others. It was followed by the study of elastic and viscoelastic layers by Nonweiler (1963) and Kaplan (1964). These works and other contemporary studies laid the main foundations of the subject. The major findings of the early works are:

(i) Wall compliance promotes the stability of the Tollmien–Schlichting instability (TSI) waves, but also introduces a host of new instabilities which are related to the compliant quality of the wall. The new instabilities are termed compliance-induced flow instabilities (CIFI) to distinguish them from the TSI which also exists on a rigid wall. The CIFI are called FISI (flow-induced surface instabilities) in the works of Carpenter and coworkers. Among the CIFI, three main types may be identified. The first two are related to the free-surface wave modes and the static deformation modes of the wall. They correspond respectively to the flutter and divergence instabilities in the field of aeroelasticity. The terms travelling-wave flutter (TWF) and static divergence (SD) are frequently used to describe these instabilities. The third type of instability is akin to the classical Kelvin–Helmholtz instability.

(ii) The instabilities are affected in different ways by wall damping. Based on energy considerations, Benjamin (1963) proposed a three-fold classification of this behaviour. In this classification, an instability is Class A if it grows as a result of energy being extracted from the system. Such instabilities are destabilized by wall damping. The TSI and divergence instability are examples of such instability. Class B instability has the opposite characterization: the instabilities associated with the free-wave modes of the wall are Class B and they are damped by wall damping. Flutter instabilities belong to this class. Belonging to the third class, Class C, are instabilities which thrive mainly on conservative exchange of energy between components of the total system. Such instabilities are not strongly influenced by wall damping. The Kelvin–Helmholtz type of instability is Class C.

With such a proliferation of instabilities and such contradictory responses to changes in wall properties, the achievement of boundary-layer stabilization appeared then to be, and still is, a highly delicate affair.

In recent years, the modelling of compliant walls has become more refined and sophisticated. Spectacular increases in computing power and progress in numerical algorithms have greatly eased and lowered the cost associated with the solution of the stability problem. Bending plates on an elastic foundation, with and without a viscous fluid substrate, were studied by Carpenter & Garrad (1985, 1986). Multi-layer viscoelastic walls were studied by Yeo (1986, 1988). Walls with an anisotropic surface response designed to induce Reynolds shear stress of predetermined sign were studied by Carpenter & Morris (1990) and Yeo (1986, 1990). Carpenter & Morris used an idealized rigid sprung-lever model while Yeo used material anisotropy in single- and two-layer arrangements. Moreover, in a recent experimental programme carried out at British Maritime Technology, Teddington, Gaster (1987) (see also Willis 1986) demonstrated convincingly that the Orr–Sommerfeld stability theory is also applicable to the compliant-wall situation. This work provided the theoretical community engaged in compliant wall research with a much needed boost of

confidence, as the Orr–Sommerfeld theory has up till now been the cornerstone of much of the theoretical work done on compliant-wall flow stability. Besides reaffirming the major findings of the earlier works, the more extensive and intensive recent studies, made possible by the availability of greatly increased computing power, have gone further to suggest strongly that significant delay of transition (from laminar to turbulent flow) may be possible with suitably designed walls/surfaces. The greater complexity of the more recent models (with a larger number of controllable parameters) has a part to play in this. It allows finer as well as more selective control to be exercised on the various instabilities, hence making it possible to suppress the CIFI while still allowing significant stabilization of the TSI to be achieved. A recent survey of compliant wall stability research was given by Riley, Gad-el-Hak & Metcalfe (1988).

Most of the work done on compliant-wall flow stability has, however, been devoted to the case of two-dimensional (2D) disturbances. These are associated with wave propagation in the stream direction. There appear to be two reasons for this preoccupation with the 2D case instead of the more general three-dimensional (3D) case involving oblique wave propagation: first the relative simplicity of the former; and secondly the fact that for a rigid wall, the reference case with respect to which gains in stability are usually assessed, the critical Reynolds number and the most dominant/rapidly growing disturbance modes are given by 2D modes, in accordance with Squire's theorem (Drazin & Reid 1981). Existing knowledge concerning 3D/oblique wave modes in flow over compliant walls is rather limited. Although 2D studies have been successful in elucidating the important mechanics associated with compliant-wall flow stability, progress in boundary-layer studies, both theoretical and experimental, has indicated that continued preoccupation with the 2D case is both unjustified and undesirable.

For a rigid wall, the tendency of the instability in boundary layers to develop three-dimensionality has been well established since the experimental work of Klebanoff, Tidstrom & Sargent (1962). Recent experimental studies such as those of Saric & Thomas (1984) and Kachanov & Levchenko (1984), employing the same vibrating-ribbon technique, have also added considerably to our knowledge of the three-dimensional events that go on in an unstable boundary layer. In the realm of linear stability theory, Mack (1978) noted that although the most unstable wave at a given Reynolds number is 2D, the most rapidly downstream growing instability wave driven at a fixed frequency may well be 3D. This result suggests that three-dimensional linear modes may yet play a fundamental role in the creation of three-dimensionality in an unstable boundary layer, possibly complementing those of nonlinear effects. In fact, aside from their possible importance in the linear context, 3D modes also play a primary function in the resonant triad theory of Craik (1971), which was postulated to explain the spanwise structures observed in the experiments of Klebanoff *et al.* Three-dimensional linear modes are also fundamental to the linear resonant interaction theory of Gustavsson & Hultgren (1980). As another example illustrating the important role played by the 3D linear modes, we should also mention that Gaster (1975) successfully modelled the spatial and temporal evolution of an experimentally observed wave packet in the earlier stages of its growth using a Fourier synthesis of 2D and 3D linear modes. Detailed comparison between the experimental and the theoretically synthesized pulses revealed that nonlinear effects, which led to generation of superimposed higher frequency modes, had generally been weak during much of the growth of the wave packet.

The above serves merely to emphasize the fundamental importance of 3D/oblique

wave modes in the instability of two-dimensional boundary layers and that the instability is characterized by a strong degree of three-dimensionality even when the most dominant modes are supposedly 2D. Similarly for compliant walls there are no *a priori* grounds to suppose that the most unstable mode will be 2D. In fact, it can be shown, via a rotation of the coordinate frame, that 3D temporal disturbances in a 2D basic flow field always perceive a basic velocity field of reduced magnitude. While this generally has the desirable effect on flow stability of reducing the effective Reynolds number of the perceived flow, it also has the effect of making the compliant wall appear stiffer to the flow. The notion that oblique wave modes perceive a wall with reduced compliance relative to the 2D case was pointed out by Yeo (1986), and is termed the *stiffness rescaling* effect in the subsequent discussion. This idea was also emphasized by Carpenter & Morris (1989). In the case of the TSI, the perceived increase in wall stiffness can be expected to have a destabilizing influence, as earlier 2D studies has shown. With the simultaneous presence of two opposing influences on stability, it becomes more difficult to know, without actual calculation, if the 2D or the 3D modes are going to be the more unstable ones. Squire's theorem, which is based only on the effective reduction in the Reynolds number for 3D/oblique modes, obviously could not be expected to remain valid. In fact, the existence of a destabilizing influence on stability, not present in the case of a rigid wall, strongly indicates that 3D disturbance modes will play a more important role in the stability of flows over compliant walls than in similar flows over rigid walls. The problem concerning the relative dominance of 2D and 3D modes gets more complex when the surface/wall exhibits an anisotropic response with respect to the direction of wave propagation. There are good reasons for studying walls which respond anisotropically to surface stresses. Firstly, some of the walls which have shown a highly favourable influence on flow stability in 2D studies are anisotropic (Yeo 1990). Secondly, anisotropy may provide a facility by which the stability of oblique wave modes may be favourably influenced.

Literature on the subject of 3D wave modes in flows over compliant walls is very limited. Cursory remarks concerning such modes may be found in Benjamin (1960) and Landahl (1962). Kaplan (1964) did a limited study on spring-backed membranes, but his results probably contain the errors pointed out by Carpenter & Garrad (1985). For potential flow over orthotropic plates (which admit mainly Class A CIFI) Carpenter (1984) showed that the most unstable temporal disturbance is 2D. Some 3D results for boundary-layer flow over a class of plate-type anisotropic walls were recently presented by Carpenter & Morris (1989). A more complete version of this work, which delves into the role of 3D modes in transition delay over both isotropic and anisotropic plate surfaces, is now available in Joslin, Morris & Carpenter (1991). An asymptotic theory applicable to 3D wave modes was also recently presented by Carpenter & Gajjar (1990), and applied to plate-type surfaces. A detailed and comprehensive study of 3D wave modes was undertaken by Yeo (1986), wherein cases of both isotropic- and anisotropic-material (single- and multi-layered) walls were examined.

The multi-layer walls studied by Yeo (1986) were modelled using well-established linear continuum mechanics of solids. The theory admits three degrees of freedom for the displacement at each point in the wall, and caters naturally for anisotropic-material behaviour of the most general type. The latter is an important feature because of the increasing availability of anisotropic materials in composite or other forms. The theory provides a highly realistic simulation of the dynamical behaviour of compliant walls constructed from one or more solid layers, subject to the

assumption that the displacement is small. Carpenter (1990) called such modelling a *volume-based* method. Surface models such as membranes and plates admit essentially one degree of freedom in displacement. They tend to be simpler in dynamics, but nevertheless contain all the primary dynamical ingredients of the more complex volume-based models: inertia, elasticity and damping. Thus membrane tension and spring foundation stiffness are the counterparts of stiffness moduli and thickness of solid layers; foundation damping is the counterpart of viscoelastic material damping and membrane surface density is the counterpart of material density. Beside these gross similarities, there are no simple relations between the parameters of surface models and the properties in layered models. The simplicity of the membrane model enabled Benjamin (1960, 1963) and Landahl (1962) to elicit the fundamental features of compliant-wall flow stability and lay the foundation for the subject. Its simplicity also allowed Carpenter and coworkers to make rapid progress in their study of the transition-delaying potential of plate surfaces. Simplicity also has its price. Thus, the plate model tends to overpredict the stiffness of the wall to disturbances of shorter wavelengths because of its inherent assumption of small thickness. And compliant surfaces of the membraneous type in particular are not very practical constructs. They tend to be rather more difficult to build and maintain to specifications for either experimental or application purposes. Walls comprising layers of say elastomeric materials are more easily constructed, and are most likely to be the form that practical compliant walls will take. Furthermore, in their multi-layer configuration, layered walls also confer a degree of control (from design viewpoint) over the stability characteristics of the flow not available to the simpler surface models. The original Kramer walls are multi-layer in construction, albeit complex because Kramer had to cater for spaces for his damping fluid. Elastomeric material layers were also used by Gal-el-Hak, Blackwelder & Riley (1984) and many others in their experimental compliant-wall studies. In his recent experimental work, directed at verifying the validity of the Orr–Sommerfeld theory applied to the compliant-wall situation (already alluded to), Gaster (1987) had in fact chosen to work with two-layer rubber walls. Excellent agreement was found between the experimentally measured amplification rates and the predictions of a corresponding two-layer volume-based model similar to those studied by Yeo (1986, 1988) (see also Willis 1986). These are justifications for studying solid-layer compliant walls. After all, to build solid-layer walls to delay laminar–turbulent transition, we would need to know the generic features of their stability behaviour as well as how to determine their precise stability characteristics.

In this paper, we shall be concerned primarily with the linear stability of 3D/oblique wave modes in zero-pressure-gradient boundary-layer flow over layered compliant walls. It represents a summary of the 3D results in Yeo (1986) with additional new results. Issues relating to the possible occurrence and consequences of wave interactions are not considered in this paper although they are very interesting in their own right and essential to a fuller understanding of flow instability and transition over compliant walls; and the possibilities for such interactions appear to be enhanced by the presence of compliant surface response. It is the author's view that these more complex problems are best deferred until we have acquired a more comprehensive knowledge of the issues concerning the linear modes.

The present study covers both isotropic and anisotropic compliant walls. The formulation of the 3D stability eigenvalue is described in §2 for the general case of a multi-layer anisotropic wall. Anisotropy with respect to the direction of wave propagation is derived from anisotropy of the wall material. The important subcase

of walls possessing an isotropic surface response is considered in detail in §2.6. Here, it is shown that the study of the unstable 3D eigenmodes can be reduced to the study of an equivalent 2D problem. Results for isotropic- and anisotropic-material walls are discussed in §§3 and 4 respectively. The 3D results supplement the 2D stability results of Yeo (1988) for isotropic-material walls and Yeo (1990) for a class of transversely isotropic-material walls. The present paper can be regarded as a sequel to these works. The use of material anisotropy to improve 3D stability is also explored.

2. Theoretical formulation

The fundamental problem of concern here is the stability of two-dimensional boundary-layer flow on compliant surfaces/walls to small-amplitude three-dimensional (oblique) disturbance waves. The coordinate frame (x_1, x_2, x_3) of the stability problem is depicted in figure 1. The x_1-axis points in the principal stream direction, while the x_2- and x_3-axes point respectively in the cross-flow and the upward vertical directions. The compliant walls of interest are assumed to be composed of one or more uniformly thick layers of homogeneous compliant materials backed by a rigid base, with the top surface spanning the (x_1, x_2)-plane at $x_3 = z_0 = 0$ in the unperturbed state. A sample two-layer anisotropic compliant wall is illustrated in figure 1. For the theoretical treatment, the compliant materials are assumed in this section to possess anisotropy of general but unspecified type.

2.1. *Governing equations and boundary conditions*

Subject to the assumptions of small-amplitude disturbances and locally parallel mean flow $\boldsymbol{U} = (U(x_3), 0, 0)^{\mathrm{T}}$, the Navier–Stokes equations and the continuity equation admit a disturbance velocity $\boldsymbol{u} = (u_1, u_2, u_3)^{\mathrm{T}}$ and disturbance pressure solutions having the form

$$(\boldsymbol{u}, p)^{\mathrm{T}} = (\hat{\boldsymbol{u}}, \hat{p})^{\mathrm{T}} \exp\left[\mathrm{i}(\alpha x_1 + \beta x_2 - \omega t)\right] \tag{1}$$

of a travelling wave propagating in the $(\alpha_{\mathrm{r}}, \beta_{\mathrm{r}}, 0)$ direction, where α and β are the x_1- and x_2-wavenumbers respectively. Subscript r denotes the real part and ω is the radian frequency. The hat symbol denotes the x_3-dependent amplitude functions. The disturbance velocity and pressure amplitude functions $\hat{\boldsymbol{u}} = (\hat{u}_1, \hat{u}_2, \hat{u}_3)^{\mathrm{T}}$ and $\hat{p}$ satisfy the following linear differential equations:

$$\mathrm{i}\alpha(U-c)\,\hat{u}_1 + U'\hat{u}_3 = -\mathrm{i}\alpha\hat{p} + R_\delta^{-1}[\hat{u}_1'' - (\alpha^2+\beta^2)\,\hat{u}_1], \tag{2a}$$

$$\mathrm{i}\alpha(U-c)\,\hat{u}_2 = -\mathrm{i}\beta\hat{p} + R_\delta^{-1}[\hat{u}_2'' - (\alpha^2+\beta^2)\,\hat{u}_2], \tag{2b}$$

$$\mathrm{i}\alpha(U-c)\,\hat{u}_3 = -\hat{p}' + R_\delta^{-1}[\hat{u}_3'' - (\alpha^2+\beta^2)\,\hat{u}_3], \tag{2c}$$

$$\mathrm{i}(\alpha\hat{u}_1 + \beta\hat{u}_2) + \hat{u}_3' = 0 \tag{2d}$$

(see §25 of Drazin & Reid 1981). The velocities, lengths and densities in (1) and (2) are assumed to have been non-dimensionalized with respect to the following reference scales: the free-stream velocity $U_\infty^{(\mathrm{d})}$, the local displacement thickness of the boundary layer $\delta^{(\mathrm{d})}$, and the density of the flow $\rho_f^{(\mathrm{d})}$. Superscript (d) indicates that the quantity is dimensional. $R_\delta = U_\infty^{(\mathrm{d})}\,\delta^{(\mathrm{d})}/\nu_f^{(\mathrm{d})}$ denotes the Reynolds number based on the local displacement thickness, where $\nu_f^{(\mathrm{d})}$ is the kinematic viscosity of the fluid. $c = \omega/\alpha$ is the phase speed of the wave in the x_1-direction. The prime denotes ordinary derivative with respect to x_3. $R_\delta = 1.72078 R_x^{\frac{1}{2}}$, where $R_x = U_\infty^{(\mathrm{d})}\,x_1^{(\mathrm{d})}/\nu_f^{(\mathrm{d})}$ is the Reynolds number based on the streamwise distance from the leading edge $x_1^{(\mathrm{d})}$. For

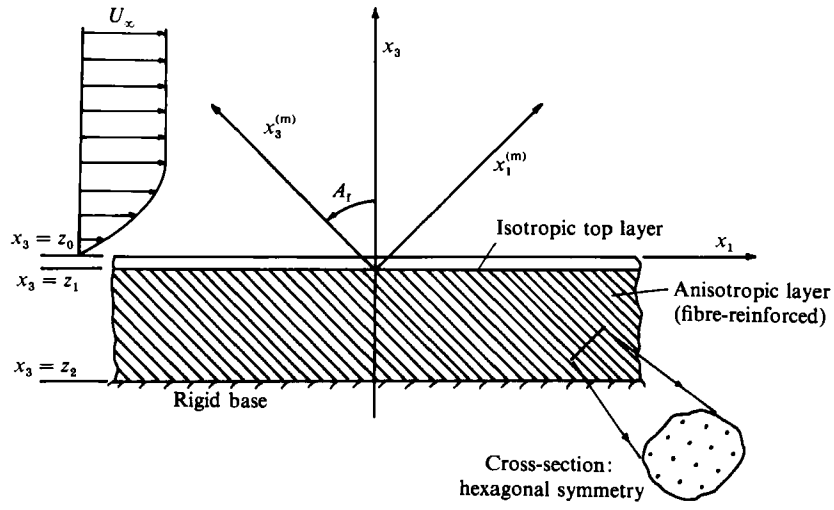

FIGURE 1. Flow over an anisotropic two-layer compliant wall. (x_1, x_2, x_3) denotes the coordinate frame of the stability problem. The compliant wall shown comprises a thin layer of isotropic material on a thick layer of transversely isotropic (of fibre-reinforced type) material, following Yeo (1990). A_f denotes the angle of inclination of the axis of isotropy (fibre axis) for the transversely isotropic layer.

the case of a zero-pressure-gradient boundary layer the mean flow velocity in the x_1-direction $U(x_3)$ is given by the Blasius profile; the x_3-component of the mean flow being neglected in the locally parallel flow approximation.

The linear wave modes in the compliant wall layers also have the form

$$\boldsymbol{\eta} = \hat{\boldsymbol{\eta}} \exp\left[\mathrm{i}(\alpha x_1 + \beta x_2 - \omega t)\right], \tag{3}$$

where $\boldsymbol{\eta} = (\eta_1, \eta_2, \eta_3)^{\mathrm{T}}$, the displacement vector, satisfies the equations of motion

$$\rho \ddot{\eta}_p = \sigma_{pq,q} \quad (p = 1, 2, 3) \tag{4}$$

and the linear anisotropic stress–strain relationship

$$\sigma_{pq} = C_{pqrs}\, \epsilon_{rs}. \tag{5}$$

Here, $[\sigma_{pq}]$ and $[\epsilon_{rs}]$ (where $\epsilon_{rs} = \frac{1}{2}(\eta_{r,s} + \eta_{s,r})$) are the stress and strain tensors respectively. $[C_{pqrs}]$ is called the viscoelastic modulus tensor here and its components are complex functions of frequency ω when there is material damping. Einstein's convention on repeated indices and subscript comma is assumed throughout this paper. The viscoelastic modulus tensor satisfies the following symmetry conditions:

$$C_{pqrs} = C_{qprs} = C_{pqsr} \quad \text{and} \quad C_{pqrs} = C_{rspq}, \tag{6}$$

see Fung (1965). These conditions reduce the number of independent components of $[C_{pqrs}]$ to a maximum of 21 for the most general homogeneous anisotropic material; see Green & Zerna (1968).

The disturbances in the flow and the wall are coupled at their common interface, whose position is not generally known in advance, by the conditions of velocity and stress continuity. Linearization based on surface amplitude enables these conditions to be applied at the position of the mean interface at $x_3 = z_0 = 0$. The linearized conditions of velocity continuity are

$$-\mathrm{i}\omega\hat{\eta}_1 = \hat{u}_1 + U'|_{z_0}\hat{\eta}_3, \quad -\mathrm{i}\omega\hat{\eta}_2 = \hat{u}_2, \quad -\mathrm{i}\omega\hat{\eta}_3 = \hat{u}_3. \tag{7a–c}$$

The linearized conditions of stress continuity at the wall are

$$\hat{\sigma}_{31} = \frac{1}{R_\delta}(\hat{u}_1' + \mathrm{i}\alpha\hat{u}_3 + U''|_{z_0}\hat{\eta}_3), \tag{8a}$$

$$\hat{\sigma}_{32} = \frac{1}{R_\delta}(\hat{u}_2' + \mathrm{i}\beta\hat{u}_3), \quad \hat{\sigma}_{33} = \frac{2}{R_\delta}\hat{u}_3' - \hat{p}, \tag{8b, c}$$

where $\hat{\sigma}_{31}$, $\hat{\sigma}_{32}$ and $\hat{\sigma}_{33}$ are the components of the traction vector $\hat{\boldsymbol{t}} = (\hat{\sigma}_{31}, \hat{\sigma}_{32}, \hat{\sigma}_{33})^{\mathrm{T}}$ acting on the wall and

$$\hat{p} = \frac{1}{R_\delta}\left(\frac{\hat{u}_3'''}{(\alpha^{\mathrm{t}})^2} - \hat{u}_3'\right) - \frac{\mathrm{i}\alpha}{(\alpha^{\mathrm{t}})^2}(U|_{z_0} - c)\,\hat{u}_3' + \frac{\mathrm{i}\alpha}{(\alpha^{\mathrm{t}})^2}U'|_{z_0}\hat{u}_3, \quad ((\alpha^{\mathrm{t}})^2 = \alpha^2 + \beta^2).$$

To complete the specification of the problem, the following boundary conditions are assumed: (i) For the wall, the last compliant layer is bonded onto the rigid base so that the displacement $\boldsymbol{\eta} = \mathbf{0}$ there. (ii) For the flow, the velocity and pressure disturbances $\boldsymbol{u}$ and p decay to zero far away from the wall.

2.2. *Transformation of governing equations and boundary conditions*

The equations and boundary conditions given in the last section fully define the stability eigenvalue problem, though not in a form that is convenient for either physical interpretation or numerical solution. Instead of using those equations directly, we formally apply a Cartesian-type transformation of the form

$$x_1^{\mathrm{t}} = \frac{\alpha}{\alpha^{\mathrm{t}}}x_1 + \frac{\beta}{\alpha^{\mathrm{t}}}x_2, \quad x_2^{\mathrm{t}} = -\frac{\beta}{\alpha^{\mathrm{t}}}x_1 + \frac{\alpha}{\alpha^{\mathrm{t}}}x_2, \quad x_3^{\mathrm{t}} = x_3, \tag{9}$$

where $(\alpha^{\mathrm{t}})^2 = \alpha^2 + \beta^2$ and $\boldsymbol{x}^{\mathrm{t}} = (x_1^{\mathrm{t}}, x_2^{\mathrm{t}}, x_3^{\mathrm{t}})$ is the coordinate vector of the new coordinate frame. The superscript t denotes quantities in the new frame. For real wavenumbers, the transformation given by (9) corresponds to a rotation of the original Cartesian frame through an angle θ about the x_3-axis where $\cos\theta = \alpha/\alpha^{\mathrm{t}}$.

Under the transformation, the flow disturbance quantities in the old and new frames are related by

$$\hat{u}_1^{\mathrm{t}} = \frac{\alpha}{\alpha^{\mathrm{t}}}\hat{u}_1 + \frac{\beta}{\alpha^{\mathrm{t}}}\hat{u}_2, \quad \hat{u}_2^{\mathrm{t}} = -\frac{\beta}{\alpha^{\mathrm{t}}}\hat{u}_1 + \frac{\alpha}{\alpha^{\mathrm{t}}}\hat{u}_2, \quad \hat{u}_3^{\mathrm{t}} = \hat{u}_3, \quad \hat{p}^{\mathrm{t}} = \hat{p}. \tag{10}$$

The linear differential equations (2) can be recombined with the pressure terms eliminated, and recast in terms of the new disturbance quantities as

$$(V - c^{\mathrm{t}})(\hat{u}_3^{\mathrm{t}\prime\prime} - (\alpha^{\mathrm{t}})^2\hat{u}_3^{\mathrm{t}}) - V''\hat{u}_3^{\mathrm{t}} = \frac{1}{\mathrm{i}\alpha^{\mathrm{t}}R_\delta}(\hat{u}_3^{\mathrm{t}\prime\prime\prime\prime} - 2(\alpha^{\mathrm{t}})^2\hat{u}_3^{\mathrm{t}\prime\prime} + (\alpha^{\mathrm{t}})^4\hat{u}_3^{\mathrm{t}}), \tag{11a}$$

$$\mathrm{i}\alpha^{\mathrm{t}}(V - c^{\mathrm{t}}) - \frac{1}{R_\delta}(\hat{u}_2^{\mathrm{t}\prime\prime} - (\alpha^{\mathrm{t}})^2\hat{u}_2^{\mathrm{t}}) = V'\frac{\beta}{\alpha}\hat{u}_3^{\mathrm{t}}, \tag{11b}$$

$$\mathrm{i}\alpha^{\mathrm{t}}\hat{u}_1^{\mathrm{t}} + \hat{u}_3^{\mathrm{t}\prime} = 0, \tag{11c}$$

where $$V(x_3^{\mathrm{t}}) = \frac{\alpha}{\alpha^{\mathrm{t}}}U(x_3) \quad \text{and} \quad c^{\mathrm{t}} = \frac{\alpha c}{\alpha^{\mathrm{t}}}.$$

Equations (11) above are identical to (46) of Stuart (1963) except for the velocity terms V and c^{t}. The velocity field $V(x_3^{\mathrm{t}})$ is merely a scaled-down version of the original

velocity field $U(x_3)$; both are referenced to the same velocity scale $U_\infty^{(d)}$. Equation (11*a*) is identical in form to the well-known Orr–Sommerfeld (OS) equation and is referred to here by the same name. Equation (11*b*) is commonly referred to as the vertical vorticity (VV) equation.

The well-known Squire's transformation (Squire 1933) is actually equivalent to the above coordinate transformation plus a further change of the reference velocity scale from $U_\infty^{(d)}$ to $V_\infty^{(d)} = U_\infty^{(d)} \cos\theta$. With this change of velocity scale, (11*a*) becomes the OS equation with the original velocity profile $U(x_3)$. The rescaled stability problem is elaborated in §3.2. For numerical implementation which involves compliant walls, however, the use of governing equations (11) with the fixed velocity reference scale $U_\infty^{(d)}$ is much to be preferred.

The formal transformation of the disturbance wall quantities follows:

$$\left.\begin{aligned} \hat{\eta}_1^t &= \frac{\alpha}{\alpha^t}\hat{\eta}_1 + \frac{\beta}{\alpha^t}\hat{\eta}_2, \quad \hat{\eta}_2^t = -\frac{\beta}{\alpha^t}\hat{\eta}_1 + \frac{\alpha}{\alpha^t}\hat{\eta}_2, \quad \hat{\eta}_3^t = \hat{\eta}_3, \\ \hat{\sigma}_{31}^t &= \frac{\alpha}{\alpha^t}\hat{\sigma}_{31} + \frac{\beta}{\alpha^t}\hat{\sigma}_{32}, \quad \hat{\sigma}_{32}^t = -\frac{\beta}{\alpha^t}\hat{\sigma}_{31} + \frac{\alpha}{\alpha^t}\hat{\sigma}_{32}, \quad \hat{\sigma}_{33}^t = \hat{\sigma}_{33}. \end{aligned}\right\} \tag{12}$$

The governing equations for wall motion (4) and the linear stress–strain relation (5) remain invariant in form under the transformation:

$$\rho \ddot{\eta}_p^t = \sigma_{pq,q}^t \quad (p = 1, 2, 3), \tag{13}$$

and

$$\sigma_{pq}^t = C_{pqrs}^t \epsilon_{rs}^t. \tag{14}$$

$[C_{pqrs}^t]$ is the modulus tensor in the transformed frame. It is related to the $[C_{ijkl}]$ of the original frame by the transformation rules for Cartesian tensors.

The interface boundary conditions given by (7) and (8), which relate the displacement and stress state of the wall at the mean interface to the disturbance quantities of the flow, can also be reformulated in terms of the transformed quantities. The transformed boundary conditions are summarized below in a matrix form that is convenient for the subsequent development of the theory:

$$\boldsymbol{S}^t(z_0) = \boldsymbol{Q}_C \boldsymbol{W}^t(z_0), \tag{15a}$$

where

$$\boldsymbol{S}^t = (\hat{\eta}_1^t, \hat{\eta}_2^t, \hat{\eta}_3^t, \hat{\sigma}_{31}^t, \hat{\sigma}_{32}^t, \hat{\sigma}_{33}^t)^T, \tag{15b}$$

$$\boldsymbol{W}^t = (\hat{u}_3^t, \hat{u}_3^{t\prime}, \hat{u}_3^{t\prime\prime}, \hat{u}_3^{t\prime\prime\prime}, \hat{u}_2^t, \hat{u}_2^{t\prime})^T, \tag{15c}$$

and

$$\boldsymbol{Q}_C = \begin{bmatrix} -\omega^{-2}V_w' & -(\alpha^t\omega)^{-1} & 0 & 0 & 0 & 0 \\ \dfrac{\beta}{\alpha\omega^2}V_w' & 0 & 0 & 0 & \mathrm{i}\omega^{-1} & 0 \\ \mathrm{i}\omega^{-1} & 0 & 0 & 0 & 0 & 0 \\ \mathrm{i}R_\delta^{-1}(\alpha^t + \omega^{-1}V_w'') & 0 & -(\mathrm{i}\alpha^t R_\delta)^{-1} & 0 & 0 & 0 \\ \dfrac{\mathrm{i}\beta}{\alpha\omega}R_\delta^{-1}V_w'' & 0 & 0 & 0 & 0 & R_\delta^{-1} \\ (\mathrm{i}\alpha^t)^{-1}V_w' & (3R_\delta^{-1} + c^t(\mathrm{i}\alpha^t)^{-1}) & 0 & -(\alpha^t)^{-2}R_\delta^{-1} & 0 & 0 \end{bmatrix}. \tag{15d}$$

$\boldsymbol{S}^t$ is termed the displacement-stress vector and $\boldsymbol{Q}_C$ the flow–wall coupling matrix. Subscript w in (15*d*) denotes evaluation of the terms at the mean interface. It is noted that $V_w'' = 0$ for the Blasius mean flow.

The requirement that the flow disturbances decay to zero as $x_3^t \to \infty$ can be translated into suitable boundary conditions for $\hat{u}_2^t$ and $\hat{u}_3^t$ by examining the exponential solutions of (11a, b) at large x_3^t. Upon discarding the exponentially growing solutions, it is easy to show that at large x_3^t the flow disturbances $\hat{u}_2^t$ and $\hat{u}_3^t$ should satisfy

$$\begin{pmatrix} \alpha^t\chi & (\alpha^t+\chi) & 1 & 0 & 1 & 0 \\ 0 & \alpha^t\chi & (\alpha^t+\chi) & 1 & 0 & 0 \\ 0 & 0 & 0 & 0 & \chi & 1 \end{pmatrix} \boldsymbol{W}^t = \boldsymbol{0}, \tag{16a–c}$$

where $\chi = [(\alpha^t)^2 + i\alpha^t R_\delta(V_\infty - c^t)]^{\frac{1}{2}}$ and $\alpha_r^t, \chi_r > 0$. The transformed boundary conditions at the rigid base are simply given by $\boldsymbol{\eta}^t = (\eta_1^t, \eta_2^t, \eta_3^t)^T = \boldsymbol{0}$.

The formulation of the eigenvalue problem is greatly simplified by the fact that (13) and (14) (or (4) and (5)) governing wall motion can be solved in closed form. This is described next.

2.3. *Wave propagation in anisotropic compliant layers*

From (3), the fundamental wave solutions to (13) and (14) for a uniformly thick homogeneous layer in the transformed variables has the form of

$$\boldsymbol{\eta}^t = \hat{\boldsymbol{\eta}}^t \exp[i(\alpha^t x_1^t - \omega t)], \tag{17}$$

where $\hat{\boldsymbol{\eta}}^t = \boldsymbol{b}\exp(i\gamma x_3^t)$. For a non-trivial wave, the substitution of (17) into (13) and (14) yields the following determinantal equation:

$$\mathrm{Det}[\rho\omega^2\delta_{ps} - C_{pqrs}^t k_q^t k_r^t] = 0, \tag{18}$$

where the wavenumbers $(k_1^t, k_2^t, k_3^t) = (\alpha^t, 0, \gamma)$ and δ_{ps} is the Kronecker delta. For a wave of specified frequency ω and wavenumbers α and β (and therefore of known α^t), (18) is a six-degree polynomial equation in γ. For simplicity, we assume the six roots of (18), denoted by $\gamma_n (n = 1, \ldots, 6)$, to be distinct. (Note that (18) is formally equivalent to the determinantal equation obtained from the substitution of (3) into (4) and (5). They have the same set of γ-roots.) The general solution to the wave propagation problem can then be represented as a linear combination,

$$\boldsymbol{\eta}^t = \sum_{n=1}^{6} D_n \boldsymbol{\eta}^{t(n)}, \tag{19a}$$

of the six fundamental solutions

$$\boldsymbol{\eta}^{t(n)} = \boldsymbol{b}^{(n)} \exp(i\gamma_n x_3^t) \exp[i(\alpha^t x_1^t - \omega t)] \quad (n = 1, \ldots, 6), \tag{19b}$$

where $\boldsymbol{b}^{(n)} = (b_{1n}, b_{2n}, b_{3n})^T$ is the eigenvector corresponding to the root γ_n. $D_n (n = 1, \ldots, 6)$ are complex constants which are determined by the boundary conditions on the layer. The x_3^t-dependent amplitudes of the components of $\boldsymbol{\eta}^t$ are

$$\hat{\eta}_p^t = \sum_{n=1}^{6} D_n b_{pn} \exp(i\gamma_n x_3^t) \quad (p = 1, 2, 3). \tag{20}$$

Substituting the solution (19) into the stress-strain relation (14), the x_3^t-dependent amplitudes of the disturbance stresses can be obtained as

$$\hat{\sigma}_{pq}^t = \frac{i}{2} \sum_{n=1}^{6} D_n C_{pqrs}^t (b_{rn} k_s^{(n)} + b_{sn} k_r^{(n)}) \exp(i\gamma_n x_3^t), \tag{21}$$

where $(k_1^{(n)}, k_2^{(n)}, k_3^{(n)}) = (\alpha^t, 0, \gamma_n)$. Note that there is summation on indices r and s in (21). With (20) and (21), the displacement and stress state at any point in a layer is

given in terms of the constants $D_n (n = 1, \ldots, 6)$. In particular, the displacement-stress vector $\boldsymbol{S}^{\mathrm{t}} = (\hat{\eta}_1^{\mathrm{t}}, \hat{\eta}_2^{\mathrm{t}}, \hat{\eta}_3^{\mathrm{t}}, \hat{\sigma}_{32}^{\mathrm{t}}, \hat{\sigma}_{33}^{\mathrm{t}})^{\mathrm{T}}$ is linearly related to the constant vector $\boldsymbol{D} = (D_1, \ldots, D_6)^{\mathrm{T}}$ as

$$\boldsymbol{S}^{\mathrm{t}}(x_3^{\mathrm{t}}) = \boldsymbol{Q}(x_3^{\mathrm{t}})\, \boldsymbol{D}, \tag{22}$$

where the components of the matrix $\boldsymbol{Q}$ may be deduced from (20) and (21).

Let us assume that the first (topmost) compliant layer spans from $x_3^{\mathrm{t}} = z_0$ (top) to $x_3^{\mathrm{t}} = z_1$ (bottom) and has thickness $h = z_0 - z_1$. The displacement-stress vector $\boldsymbol{S}^{\mathrm{t}}(z_0)$ at the top surface is then related to its value $\boldsymbol{S}^{\mathrm{t}}(z_1)$ at the bottom surface of the layer by

$$\boldsymbol{S}^{\mathrm{t}}(z_1) = \boldsymbol{P}(z_1, z_0)\, \boldsymbol{S}^{\mathrm{t}}(z_0) = \boldsymbol{P}(0, h)\, \boldsymbol{S}^{\mathrm{t}}(z_0), \tag{23}$$

where $\boldsymbol{P}(z_1, z_0) = \boldsymbol{Q}(z_1)\, \boldsymbol{Q}^{-1}(z_0)$ is termed the propagation matrix. One such propagation matrix can be defined for each homogeneous layer in a multi-layer compliant wall. In a compliant wall comprising n layers (where the jth layer spans from $x_3^{\mathrm{t}} = z_{j-1}$ (top) to $x_3^{\mathrm{t}} = z_j$ (bottom)), it is easy to see that

$$\boldsymbol{S}^{\mathrm{t}}(z_n) = \boldsymbol{P}^{\mathrm{O}} \boldsymbol{S}^{\mathrm{t}}(z_0), \tag{24a}$$

where the matrix

$$\boldsymbol{P}^{\mathrm{O}} = \prod_{j=n}^{j=1} \boldsymbol{P}^{(j)}(z_j, z_{j-1}) \tag{24b}$$

is termed the overall propagation matrix and $\boldsymbol{P}^{(j)}$ is the propagation matrix of the jth layer of the n-layer compliant wall. The overall propagation matrix relates the displacement and stress state at the top surface of the first compliant layer to the displacement and stress state at the bottom of the last compliant layer, which is assumed to be in bonded contact with the rigid base. Equation (24) represents the form of the wave solution for the wall which is useful both as a generalized formulation of the stability eigenvalue problem (applicable to a compliant wall having any finite number of layers) and for numerical implementation.

2.4. *The three-dimensional stability eigenvalue problem*

From (15) and (24), we immediately have

$$\boldsymbol{S}^{\mathrm{t}}(z_n) = \boldsymbol{P}^{\mathrm{O}} \boldsymbol{Q}_{\mathrm{C}}\, \boldsymbol{W}^{\mathrm{t}}(z_0), \tag{25}$$

which relates the displacement–stress state at the rigid-base interface to the flow disturbances at the mean flow–wall interface at $x_3^{\mathrm{t}} = z_0$. At the rigid-base interface, $\hat{\boldsymbol{\eta}}^{\mathrm{t}}(z_n) = (\hat{\eta}_1^{\mathrm{t}}, \hat{\eta}_2^{\mathrm{t}}, \hat{\eta}_3^{\mathrm{t}})^{\mathrm{T}}(z_n) = \boldsymbol{0}$, so that the first three rows of (25) yield three boundary conditions for the flow disturbance quantities $\hat{u}_2^{\mathrm{t}}$ and $\hat{u}_3^{\mathrm{t}}$. Three further boundary conditions are furnished by (16*a–c*), arising from the requirement that flow disturbances must decay to zero as $x_3^{\mathrm{t}} \to \infty$. These six homogeneous boundary conditions and the disturbance flow equations (11*a*, *b*) constitute the three-dimensional stability eigenvalue problem.

2.5. *Models of homogeneous anisotropy*

In this section, we give a precise but brief description of the homogeneous anisotropy models used in this paper. More information concerning the models and some of their physical realizations may be found in Lekhnitskii (1963) and Christensen (1979). The latter concerns anisotropy in composite materials. The constitutive stress–strain relations are given with respect to coordinate frames denoted by $(x_1^{(\mathrm{m})}, x_2^{(\mathrm{m})}, x_3^{(\mathrm{m})})$. These frames are termed *material-property* frames. With respect to its material-property frame, the stress–strain law of an anisotropic material assumes a simple

(usually with the maximum number of zeros in its modulus tensor) and physically meaningful form. Commonly used material moduli such as Young's modulus, shear modulus and Poisson's ratio are usually specified with respect to these frames; and indeed meaningful only in the context of such frames.

The stress–strain laws in other Cartesian coordinate frames, such as (x_1, x_2, x_3) and (x_1^t, x_2^t, x_3^t) of the original and the transformed stability problems respectively, can be obtained from the stress–strain law specified in the material-property frame $(x_1^{(m)}, x_2^{(m)}, x_3^{(m)})$ by the application of the transformation rules for Cartesian tensors. Thus if l_{ij} denotes the cosine of the angle between the x_i-axis of the (x_1, x_2, x_3)-frame and the $x_j^{(m)}$-axis of the $(x_1^{(m)}, x_2^{(m)}, x_3^{(m)})$-frame then the modulus tensor $[C_{pqrs}]$ in the former frame is given in terms of $[C_{ijkl}^{(m)}]$ of the latter frame by

$$C_{pqrs} = C_{ijkl}^{(m)} l_{pi} l_{qj} l_{rk} l_{sl}.$$

2.5.1. *Orthotropy*

The orthotropy model is characterized by the existence of three mutually orthogonal planes of symmetry. A *plane of symmetry* means a plane about which the properties of the material are symmetric; see Green & Zerna (1968). Nine independent moduli are required to specify the most general orthotropic material. The stress–strain relationship for an orthotropic material which has the three orthogonal planes parallel to the $(x_1^{(m)}, x_2^{(m)})$, $(x_2^{(m)}, x_3^{(m)})$- and $(x_1^{(m)}, x_3^{(m)})$-planes of the material-property frame assumes the following compact form:

$$[\sigma_{11}, \sigma_{22}, \sigma_{33}, \sigma_{23}, \sigma_{13}, \sigma_{12}]^{T(m)} = \boldsymbol{C}^{(m)} [\epsilon_{11}, \epsilon_{22}, \epsilon_{33}, 2\epsilon_{23}, 2\epsilon_{13}, 2\epsilon_{12}]^{T(m)}, \tag{26a}$$

where

$$\boldsymbol{C}^{(m)} = \begin{pmatrix} C_{1111}^{(m)} & C_{1122}^{(m)} & C_{1133}^{(m)} & 0 & 0 & 0 \\ C_{1122}^{(m)} & C_{2222}^{(m)} & C_{2233}^{(m)} & 0 & 0 & 0 \\ C_{1133}^{(m)} & C_{2233}^{(m)} & C_{3333}^{(m)} & 0 & 0 & 0 \\ 0 & 0 & 0 & C_{2323}^{(m)} & 0 & 0 \\ 0 & 0 & 0 & 0 & C_{1313}^{(m)} & 0 \\ 0 & 0 & 0 & 0 & 0 & C_{1212}^{(m)} \end{pmatrix}. \tag{26b}$$

The components of matrix $\boldsymbol{C}^{(m)}$ are derived directly from the components of the modulus tensor $[C_{ijkl}^{(m)}]$. For simplicity, stress–strain relations for anisotropic models are frequently presented in their *compliance* form:

$$[\epsilon_{11}, \epsilon_{22}, \epsilon_{33}, 2\epsilon_{23}, 2\epsilon_{13}, 2\epsilon_{12}]^{T(m)} = \boldsymbol{S}^{(m)} [\sigma_{11}, \sigma_{22}, \sigma_{33}, \sigma_{23}, \sigma_{13}, \sigma_{12}]^{T(m)} \tag{27}$$

where $\boldsymbol{S}^{(m)} = [\boldsymbol{C}^{(m)}]^{-1}$, the matrix inverse of $\boldsymbol{C}^{(m)}$. The compliance matrix $\boldsymbol{S}^{(m)}$ for an orthotropic model is given by

$$\boldsymbol{S}^{(m)} = \begin{pmatrix} \frac{1}{E_1} & -\frac{\nu_{12}}{E_1} & -\frac{\nu_{13}}{E_1} & 0 & 0 & 0 \\ -\frac{\nu_{21}}{E_2} & \frac{1}{E_2} & -\frac{\nu_{23}}{E_2} & 0 & 0 & 0 \\ -\frac{\nu_{31}}{E_3} & -\frac{\nu_{32}}{E_3} & \frac{1}{E_3} & 0 & 0 & 0 \\ 0 & 0 & 0 & \frac{1}{G_{23}} & 0 & 0 \\ 0 & 0 & 0 & 0 & \frac{1}{G_{13}} & 0 \\ 0 & 0 & 0 & 0 & 0 & \frac{1}{G_{12}} \end{pmatrix}. \tag{28}$$

E_i is the Young's modulus of the material along the $x_i^{(m)}$-axis; ν_{ij} is the Poisson's ratio characterizing the contraction along the $x_j^{(m)}$-axis when the material is subjected to imposed strain along the $x_i^{(m)}$-axis. We note that the compliance matrix $\boldsymbol{S}^{(m)}$ is a symmetric matrix so that $\nu_{ij}E_j = \nu_{ji}E_i$ (no sum on indices). G_{ij} is the shear modulus for shear deformation (divergence free) in the $(x_i^{(m)}, x_j^{(m)})$-plane.

2.5.2. *Transverse isotropy*

The transverse isotropy model is characterized by the existence of a distinguished direction, termed the *axis of isotropy*. The properties of the material are identical in all directions perpendicular to this axis, and planes normal to this axis are called *planes of isotropy*. Five independent moduli are required to specify the most general form of transverse isotropy. With the axis of isotropy aligned along the $x_3^{(m)}$-axis of the material-property frame, the compliance matrix has the form

$$\boldsymbol{S}^{(m)} = \begin{pmatrix} \frac{1}{E} & -\frac{\nu}{E} & -\frac{\nu'}{E'} & 0 & 0 & 0 \\ -\frac{\nu}{E} & \frac{1}{E} & -\frac{\nu'}{E'} & 0 & 0 & 0 \\ -\frac{\nu'}{E'} & -\frac{\nu'}{E'} & \frac{1}{E'} & 0 & 0 & 0 \\ 0 & 0 & 0 & \frac{1}{G'} & 0 & 0 \\ 0 & 0 & 0 & 0 & \frac{1}{G'} & 0 \\ 0 & 0 & 0 & 0 & 0 & \frac{1}{G} \end{pmatrix}, \tag{29}$$

where $E = 2G(1+\nu)$. E' is the Young's modulus along the axis of isotropy; G is the shear modulus for shear deformations that occur in the plane of isotropy, while G' is the shear modulus for planes normal to the plane of isotropy; and ν' is the Poisson's ratio characterizing contraction in the plane of isotropy for imposed strain along the axis of isotropy, while ν is the Poisson's ratio characterizing contraction within the plane of isotropy for imposed strain in the same plane. Transverse isotropy can be regarded as a special case of orthotropy which has one isotropy plane among its symmetry planes.

2.5.3. *Isotropy*

Complete material isotropy, meaning identical properties in all three dimensional directions, is obtained when we set $E = E'$, $\nu' = \nu$ and $G' = G$ in the transverse isotropy model. Isotropic material behaviour can also be derived from the orthotropy model by setting all the Young's moduli to E, all the shear moduli to G, all Poisson's ratios to ν, and requiring that $E = 2G(1+\nu)$. The deformation of an isotropic material subjected to stresses is characterized by just two independent moduli. The shear modulus G and bulk modulus K are commonly used. In terms of G and K, the Poisson's ratio and Young's modulus for isotropic materials are given by

$$\nu = \frac{3K-2G}{2(3K+G)}, \quad E = \frac{9KG}{3K+G}. \tag{30a, b}$$

The isotropic stress–strain relation is identical in all Cartesian reference frames. The moduli consequently have the same values in all such frames.

2.6. *Material isotropy in the* (x_1, x_2)*-plane*

In this section we focus attention on the case of compliant walls which have material properties such that the (x_1, x_2)-plane is a plane of isotropy; that is, the properties of the wall are identical with respect to all directions in the (x_1, x_2)-plane. The x_3-axis is then an axis of isotropy and all planes normal to the (x_1, x_2)-plane are planes of symmetry. Typical examples are walls constructed from layers of isotropic or transversely isotropic materials – in the latter case the materials' axis of isotropy must clearly be parallel to the x_3-axis. The objective of this section is to show that for such walls, the three-dimensional eigenvalue problem formulated in the preceding sections is reducible to an equivalent two-dimensional problem associated with the Orr–Sommerfeld equation (11*a*) for a scaled-down basic flow field.

We begin by noting that the dynamic response of the surface of the compliant wall to surface traction $\hat{\boldsymbol{t}}^{\mathrm{t}} = (\hat{\sigma}^{\mathrm{t}}_{31}, \hat{\sigma}^{\mathrm{t}}_{32}, \hat{\sigma}^{\mathrm{t}}_{33})^{\mathrm{T}}$ can be cast in the form

$$\hat{\boldsymbol{t}}^{\mathrm{t}}(z_0) = \boldsymbol{Z}^{\mathrm{t}} \hat{\boldsymbol{\eta}}^{\mathrm{t}}(z_0) \tag{31a}$$

where $\boldsymbol{Z}^{\mathrm{t}}$, a 3×3 matrix function of ω, α, β and the material properties of the wall, is given by

$$\boldsymbol{Z}^{\mathrm{t}} = \begin{bmatrix} P^{\mathrm{o}}_{14} & P^{\mathrm{o}}_{15} & P^{\mathrm{o}}_{16} \\ P^{\mathrm{o}}_{24} & P^{\mathrm{o}}_{25} & P^{\mathrm{o}}_{26} \\ P^{\mathrm{o}}_{34} & P^{\mathrm{o}}_{35} & P^{\mathrm{o}}_{36} \end{bmatrix}^{-1} \begin{bmatrix} P^{\mathrm{o}}_{11} & P^{\mathrm{o}}_{12} & P^{\mathrm{o}}_{13} \\ P^{\mathrm{o}}_{21} & P^{\mathrm{o}}_{22} & P^{\mathrm{o}}_{23} \\ P^{\mathrm{o}}_{31} & P^{\mathrm{o}}_{32} & P^{\mathrm{o}}_{33} \end{bmatrix}. \tag{31b}$$

Equation (31) is obtained from (24) by applying the boundary condition $\hat{\boldsymbol{\eta}}^{\mathrm{t}}(z_n) = \boldsymbol{0}$ at the interface with the rigid base. P^{o}_{ij} denotes the (i,j)-component of the overall propagation matrix $\boldsymbol{P}^{\mathrm{o}}$.

We next consider the form that $\boldsymbol{Z}^{\mathrm{t}}$ must assume given the symmetry with respect to all directions in the (x_1, x_2)-plane. Let us consider a wave propagating in the $(\alpha, \beta, 0)$-direction, where α and β may be assumed to be real for ease of interpretation. The x^{t}_1-axis points in this direction and the $(x^{\mathrm{t}}_1, x^{\mathrm{t}}_3)$-plane is a plane of symmetry for material properties. When the $(x^{\mathrm{t}}_1, x^{\mathrm{t}}_3)$-plane is a plane of symmetry, the fundamental wave solutions for the wall can be divided into two classes: a class of two-dimensional motion with displacement occurring only in that plane ($\hat{\eta}^{\mathrm{t}}_2 = 0$) (in-plane motion) and a class of one-dimensional motion with displacement taking place only in the x^{t}_2-direction ($\hat{\eta}^{\mathrm{t}}_1 = \hat{\eta}^{\mathrm{t}}_3 = 0$) (anti-plane motion). The wave solutions and the associated stresses of the two classes are independent of each other or, in other words, the two classes of motions are completely decoupled. An example of such a decomposition into the two distinct classes of motion, in-plane and anti-plane, due to a plane of symmetry can be found in Yeo (1990). Since the dynamics of the in-plane and anti-plane motions are decoupled from each other, the matrix $\boldsymbol{Z}^{\mathrm{t}}$ must necessarily have form

$$\boldsymbol{Z}^{\mathrm{t}} = \begin{bmatrix} Z^{\mathrm{t}}_{11} & 0 & Z^{\mathrm{t}}_{13} \\ 0 & Z^{\mathrm{t}}_{22} & 0 \\ Z^{\mathrm{t}}_{31} & 0 & Z^{\mathrm{t}}_{33} \end{bmatrix}, \tag{32}$$

where all components with indices containing the number 2 once are zero. The form of $\boldsymbol{Z}^{\mathrm{t}}$ remains the same when α and β are complex because the formal mathematical operations involved are identical to those for real α and β. A more detailed proof that $\boldsymbol{Z}^{\mathrm{t}}$ has the form given by (32) can be obtained by considering the effect of the symmetry on the governing equations and the resultant effect on the form of the propagation matrices.

From (15*a*) we have

$$\hat{\boldsymbol{\eta}}^{\mathrm{t}}(z_0) = \boldsymbol{Q}_{\mathrm{C}}^{\mathrm{U}}\, \boldsymbol{W}^{\mathrm{t}}(z_0) \quad \text{and} \quad \hat{\boldsymbol{t}}^{\mathrm{t}}(z_0) = \boldsymbol{Q}_{\mathrm{C}}^{\mathrm{L}}\, \boldsymbol{W}^{\mathrm{t}}(z_0), \tag{33a, b}$$

where $\boldsymbol{Q}_{\mathrm{L}}^{\mathrm{U}}$ and $\boldsymbol{Q}_{\mathrm{C}}^{\mathrm{L}}$ denote the upper and lower halves of the flow–wall coupling matrix $\boldsymbol{Q}_{\mathrm{C}}$ respectively. The substitution of (33) into (31) yields

$$[\boldsymbol{Q}_{\mathrm{C}}^{\mathrm{L}} - \boldsymbol{Z}^{\mathrm{t}} \boldsymbol{Q}_{\mathrm{C}}^{\mathrm{U}}]\, \boldsymbol{W}^{\mathrm{t}}(z_0) = 0. \tag{34}$$

Equation (34) is equivalent to the three wall-related boundary conditions for the eigenvalue problem of §2.5, obtained there by setting $\hat{\boldsymbol{\eta}}^{\mathrm{t}}(z_n) = \boldsymbol{0}$ in (25). The three-dimensional stability eigenvalue problem is therefore alternatively defined by the boundary conditions (16) and (34), and the flow disturbance equations (11*a*, *b*). With the restriction on the form of $\boldsymbol{Z}^{\mathrm{t}}$ given by (32), equation (34) works out as

$$\left[\frac{V_{\mathrm{w}}'}{\omega^2} Z_{11}^{\mathrm{t}} - \frac{\mathrm{i}}{\omega} Z_{13}^{\mathrm{t}} + \frac{\mathrm{i}}{R_\delta}\left(\alpha^{\mathrm{t}} + \frac{V_{\mathrm{w}}''}{\omega}\right)\right] \hat{u}_3^{\mathrm{t}} + \frac{1}{\alpha^{\mathrm{t}}\omega} Z_{11}^{\mathrm{t}}\, \hat{u}_3^{\mathrm{t}\prime} - \frac{1}{\mathrm{i}\alpha^{\mathrm{t}} R_\delta} \hat{u}_3^{\mathrm{t}\prime\prime} = 0, \tag{35a}$$

$$\frac{\beta}{\alpha^{\mathrm{t}}}\left(-\frac{V_{\mathrm{w}}'}{\omega^2} Z_{22}^{\mathrm{t}} + \frac{\mathrm{i} V_{\mathrm{w}}''}{\omega R_\delta}\right) \hat{u}_3^{\mathrm{t}} - \frac{\mathrm{i}}{\omega} Z_{22}^{\mathrm{t}}\, \hat{u}_2^{\mathrm{t}} + \frac{1}{R_\delta} \hat{u}_2^{\mathrm{t}\prime} = 0, \tag{35b}$$

$$\left(\frac{V_{\mathrm{w}}'}{\omega^2} Z_{31}^{\mathrm{t}} - \frac{\mathrm{i}}{\omega} Z_{33}^{\mathrm{t}} + \frac{V_{\mathrm{w}}'}{\mathrm{i}\alpha^{\mathrm{t}}}\right) \hat{u}_3^{\mathrm{t}} + \left(\frac{1}{\alpha^{\mathrm{t}}\omega} Z_{31}^{\mathrm{t}} + \frac{3}{R_\delta} - \frac{\mathrm{i}\omega}{(\alpha^{\mathrm{t}})^2}\right) \hat{u}_3^{\mathrm{t}\prime} - \frac{1}{(\alpha^{\mathrm{t}})^2 R_\delta} \hat{u}_3^{\mathrm{t}\prime\prime\prime} = 0. \tag{35c}$$

Careful examination of the system of equations comprising the flow disturbance equations (11*a*, *b*), the wall-related boundary conditions (35*a*–*c*) and the far-field boundary conditions (16*a*–*c*) reveals that they can be conveniently separated into two distinct subsystems. The first subsystem consists of the OS equation (11*a*) and the four boundary conditions (16*a*, *c*) and (35*a*, *c*). This is a complete system of homogeneous equations and boundary conditions in the disturbance component $\hat{u}_3^{\mathrm{t}}$ and it consequently defines an eigenvalue problem for the existence of non-trivial $\hat{u}_3^{\mathrm{t}}$-disturbances. The second subsystem comprising the VV equation (11*b*) and the two boundary conditions (16*b*) and (35*b*) is an inhomogeneous system in $\hat{u}_2^{\mathrm{t}}$ when $\beta \neq 0$ (oblique modes) and $\hat{u}_3^{\mathrm{t}} \not\equiv 0$. The second subsystem yields a solution for $\hat{u}_2^{\mathrm{t}}$ when the eigenfunction $\hat{u}_3^{\mathrm{t}}$ is prescribed by the solution of the first subsystem. The second subsystem, however, becomes homogeneous when $\hat{u}_3^{\mathrm{t}} \equiv 0$, and hence constitutes an eigenvalue problem for the existence of non-trivial disturbances with zero x_3^{t}-component. By the continuity relation (11*c*), $\hat{u}_3^{\mathrm{t}} \equiv 0$ implies $\hat{u}_1^{\mathrm{t}} \equiv 0$ so that the disturbance modes associated with the second subsystem are essentially one-dimensional motions. The disturbance modes associated with the first subsystem are three-dimensional in both the original and the transformed coordinate frames. The underlying dynamics is, however, two-dimensional, being governed by a modified OS equation and a two-dimensional set of boundary conditions.

The above analysis indicates that the three-dimensional stability eigenvalue relation for two-dimensional boundary-layer-type flows over 'isotropically' responding surfaces can be factorized into a part which is governed by the modified OS equation and a part governed by the VV equation. The same decomposition of the three-dimensional spectra is also applicable to similar flows over a rigid wall. In fact, the resonant interaction theory proposed by Gustavsson & Hultgren (1980) to explain the onset of instability in plane Couette flow concerns precisely the resonant excitation of the VV modes (second subsystem) by the $\hat{u}_3^{\mathrm{t}}$-eigenfunctions of the OS modes (first subsystem). We shall not be concerned here, however, with the possible generation of instabilities by such a mechanism; although the possibilities for interaction would appear to be enhanced by the proliferation of modes accompanying

compliant surface response. Such studies are better deferred until we have acquired an improved knowledge of the basic issues related to simple three-dimensional exponential instabilities.

For a rigid wall, the spectrum of the VV equation (11*b*) is known to comprise only damped modes (Davey & Reid 1977). From the viewpoint of linear stability theory, this spectrum is of no interest because the linear theory only provides sufficient conditions for instability. Below, it is established that the spectrum of the VV equation for the case of compliant wall possessing the usual properties of mass inertia, elasticity and viscous damping also comprises only damped modes.

In the absence of forcing by the OS modes, the VV equation is

$$\hat{u}_2^{t\prime\prime} - (\alpha^t)^2 \hat{u}_2^t - i\alpha^t (V - c^t) R_\delta \hat{u}_2^t = 0. \tag{36}$$

Multiply (36) by $\hat{u}_2^{t*}$ (where superscript * denotes complex conjugation) and integrate over the flow domain to yield

$$\int_{z_0}^{\infty} |\hat{u}_2^{t\prime}|^2 \, dx_3^t + \int_{z_0}^{\infty} [(\alpha^t)^2 + i\alpha^t (V - c^t) R_\delta] \, |\hat{u}_2^t|^2 \, dx_3^t + \hat{u}_2^{t\prime} \hat{u}_2^{t*}|_{z_0} = 0, \tag{37}$$

where the assumption that $\hat{u}_2^t \to 0$ as $x_3^t \to \infty$ has been used. In the absence of forcing, the boundary term in (37) becomes

$$\hat{u}_2^{t\prime} \hat{u}_2^{t*}|_{z_0} = i\omega^* R_\delta (\hat{\sigma}_{32}^t \hat{\eta}_2^{t*})_{z_0} \tag{38}$$

by the application of the interface boundary conditions (15). The bracketed term on the right-hand side of (38) represents work done at the mean boundary of the wall by the flow disturbance. This work-done term can be related to the dynamics of the wall in a very general manner following the variational treatment of Yeo & Dowling (1987). From (2.8*a*) of Yeo & Dowling,

$$\sigma_{32}^t \hat{\eta}_2^{t*}|_{z_0} = -2\omega^2 I + 2E - 2i\omega D, \tag{39}$$

where it is noted that the VV modes only involved the anti-plane component $\hat{\eta}_2^t$. The terms I and D are positive-definite real-valued integrals related respectively to the kinetic energy and dissipation within the compliant wall. The real-valued integral E is related directly to the stored energy within the wall and may be assumed to be positive for linear wave problems which involve small initial displacements. More details concerning the integrals are given in Yeo & Dowling (1987). The only property of I, D and E that we need to invoke here is their positivity. With (38) and (39), (37) becomes

$$\int_{z_0}^{\infty} |\hat{u}_2^{t\prime}|^2 + [(\alpha^t)^2 + i\alpha^t (V - c^t) R_\delta] \, |u_2^t|^2 \, dx_3^t = 2R_\delta (i\omega |\omega|^2 I - i\omega^* E - |\omega|^2 D). \tag{40}$$

Let us consider the case of temporal instability for which the wavenumbers α and β are real while frequency ω is allowed to be complex. α^t and $\alpha^t V = \alpha U$ are then real and $\omega_i > 0$ for unstable modes. Taking the real part of (40) we have

$$\int_{z_0}^{\infty} |\hat{u}_2^{t\prime}|^2 + [(\alpha^t)^2 + \omega_i R_\delta] \, |\hat{u}_2^t|^2 \, dx_3^t = -2R_\delta (\omega_i |\omega|^2 I + \omega_i E + |\omega|^2 D). \tag{41}$$

A simple *reductio ad absurdum* argument applied to (41) then shows that ω_i must necessarily be less than zero for non-trivial disturbance modes. The temporal eigenvalue spectrum of the system of VV equations and associated boundary conditions therefore comprises only decaying modes. This result implies, by the time-

asymptotic stability analysis of Briggs (1964), that there can neither be absolute nor convective (spatially growing casual mode) instabilities.

The above demonstrates that in studying the three-dimensional linear instability of two-dimensional boundary-layer flow over isotropically responding surfaces, we need only examine the eigenvalue spectrum of the OS equation (11*a*) and its associated boundary conditions. The problem is in essence two-dimensional and can be solved using codes designed for two-dimensional studies.

The reduction of the three-dimensional eigenvalue problem to an equivalent two-dimensional one is not generally possible for anisotropically responding surfaces. For a surface whose response is not isotropic with respect to directions in the (x_1, x_2)-plane, the components Z^t_{12}, Z^t_{21}, Z^t_{23} and Z^t_{32} of the matrix $\boldsymbol{Z}^t$ may not be zero. In particular, when Z^t_{12} is not zero, the surface traction components $\hat{\sigma}^t_{31}|_{z_0}$ and $\hat{\sigma}^t_{33}|_{z_0}$ have a dependence on the transverse displacement component $\hat{\eta}^t_2|_{z_0}$. This provides a feedback route by which the transverse disturbances $\hat{u}^t_2$ and $\hat{\eta}^t_2$ can influence the in-plane components $\hat{u}^t_1$, $\hat{u}^t_3$, $\hat{\eta}^t_1$ and $\hat{\eta}^t_3$, and hence couples the first and second subsystems of equations in a non-trivial manner. For isotropically responding surfaces, the influence only travels one way from the in-plane to the anti-plane components. An alternative explanation for the reduction of the three-dimensional eigenvalue problem to two dimensions was given in Chapter 5 of Yeo (1986) for the case of isotropic material walls.

2.7. *Aspects of numerical solutions*

For cases which are reducible to two-dimensional ones, available two-dimensional programs can be easily adapted to determine the eigenvalues; only a scaling of the mean-flow field $U(x_3)$ by the factor α/α^t is required. The 3D isotropic-wall results presented in this paper were therefore obtained by using a modified version of the 2D program of Yeo (1988) which incorporated the scaling. The $\hat{u}^t_2$-eigenfunction if required can be obtained by solving the VV equation (11*b*) and associated boundary conditions subject to forcing by the two-dimensional solution.

For the fully three-dimensional cases, which require the simultaneous solution of the OS equation (11*a*) and the VV equation (11*b*), a collocation method based on the expansion of the solutions in terms of Chebyshev polynomials was used. The mean-flow velocity and its derivatives were represented as Chebyshev series of 40 or 50 terms each. The number of Chebyshev polynomials used to represent the solutions $\hat{u}^t_2$ and $\hat{u}^t_3$ ranged from 30 for R_δ less than 1000 to more than 50 for R_δ greater than 6000. Regular checks were made to ensure that a sufficient number of terms were used. As expected, the 3D spectral collocation program was used mainly for cases which involved anisotropic materials since isotropic wall results could be obtained much more cheaply using modified 2D programs. The correctness and the accuracy of the 3D program were verified against the 2D results of Yeo (1988, 1990) (for isotropic- and anisotropic-material layered walls respectively) and the 3D results of a modified 2D isotropic-layer program. Excellent agreement, to 5 or 6 significant digits in the eigenvalues, was obtained in most cases.

The compound matrix method used to obtain the results presented in Yeo (1988, 1990) could also be adapted to solve the 3D flow stability equations. However, its application would involve the derivation of a 20×20 compound matrix. The task of deriving the components of such a large matrix analytically is both daunting and error-prone. Moreover, the polynomial expansion approach has the important advantage over the compound matrix method that the eigenfunctions are automatically determined with the eigenvalues.

The material properties of the compliant walls are specified with respect to the velocity scale $U_\infty^{(d)}$, the density scale $\rho_f^{(d)}$ and a fixed lengthscale $L_w^{(d)}$ termed the *wall* lengthscale. The velocity and density scales are identical to those employed for the flow quantities. For the flow, the lengthscale is the local displacement thickness $\delta^{(d)}$, which varies with the Reynolds number R_δ. The wall lengthscale $L_w^{(d)}$ is defined implicitly through the specification of a reference Reynolds number $R_w = U_\infty^{(d)} L_w^{(d)} / \nu_f^{(d)}$. In numerical implementation, the overall propagation matrix $\boldsymbol{P}^O$ (which contains the wall dynamics) is actually computed in the wall lengthscale rather than the flow lengthscale. In fact the $\boldsymbol{P}^O$ in the two lengthscales are related as follows

$$\boldsymbol{P}^O = \boldsymbol{M}_S^{-1} \boldsymbol{P}^{O(w)} \boldsymbol{M}_S. \tag{42}$$

The superscript w denotes computation with respect to the lengthscale $L_w^{(d)}$ and $\boldsymbol{M}_S$ is the diagonal matrix Diag $\{r, r, r, 1, 1, 1\}$ (where $r = R_\delta / R_w$) which effects the change of lengthscale. With (42), the numerical implementation of the boundary conditions (25) is based on

$$\boldsymbol{S}^{t(w)}(z_n) = \boldsymbol{P}^{O(w)} \boldsymbol{M}_S \boldsymbol{Q}_C \boldsymbol{W}^t(z_0). \tag{43}$$

This implementation has the advantage over one in which $\boldsymbol{P}^O$ is calculated in the flow lengthscale that the material properties and layer thickness of the wall need not be rescaled when the Reynolds number R_δ is changed. The reference Reynolds number R_w is set to 2×10^4 for all the results presented in this paper.

3. Isotropic-material compliant walls

In this section, we consider the case of compliant walls which are constructed from one or more uniformly thick layers of isotropic material. The two-dimensional stability of the Blasius boundary layer over such walls has been comprehensively studied by Yeo (1988). The 2D study indicates that these walls have significant potential for flow stabilization and that suitably designed ones also offer prospects for substantial delay of transition. The stability of the same flow to three-dimensional oblique wave modes is examined below.

3.1. *Specification of material properties*

The mechanical response of isotropic materials to stresses is governed by two moduli, the shear modulus G and the bulk modulus K (§2.5.3). Material damping is introduced by assuming a Kelvin–Voigt model for the shear modulus G. Dilatational (shear-free) deformation is assumed to be elastic so that the bulk modulus K is a real constant. The shear modulus is expressed in terms of the material's elastic shear wave speed C_t and a damping coefficient d as

$$G = \rho C_t^2 - i\omega d, \tag{44}$$

where the density ρ is assumed to be equal to that of the flow in all cases. The properties of the isotropic material are therefore determined here by the real parameters C_t, d and K. These are specified based on non-dimensionalization with respect to wall reference scales:

$$C_t = \frac{C_t^{(d)}}{U_\infty^{(d)}}, \quad d = \frac{d^{(d)}}{\rho_f^{(d)} U_\infty^{(d)} L_w^{(d)}}, \quad K = \frac{K^{(d)}}{\rho_f^{(d)} [U_\infty^{(d)}]^2}. \tag{45a–c}$$

The thicknesses of the compliant layers are non-dimensionalized by the wall lengthscale $L_w^{(d)}$.

3.2. *The rescaled equivalent two-dimensional problem*

In studying the linear stability of oblique wave (3D) modes, $\exp[\mathrm{i}(\alpha x_1+\beta x_2-\omega t)]$, in flows over isotropic-material compliant walls, §2.6 immediately tells us that we need only consider the eigenvalue spectrum of the equivalent 2D problem comprising the OS equation (11*a*), with the scaled-down basic velocity field $V(x_3^{\mathrm{t}}) = U(x_3)\cos\theta$, and associated boundary conditions. The instability of a 3D mode is determined only by the instability of its in-plane motion.

Let us now rescale the equivalent 2D problem using the free-stream speed of its scaled-down velocity field $V_\infty^{(\mathrm{d})} = U_\infty^{(\mathrm{d})}\cos\theta$ as the reference velocity scale. We note that the value of $V_\infty^{(\mathrm{d})}$ depends on θ. The OS equation (11*a*) then becomes

$$(U-c)(\tilde{u}_3''-(\alpha^{\mathrm{t}})^2\tilde{u}_3)-U''\tilde{u}_3 = \frac{1}{\mathrm{i}\alpha^{\mathrm{t}}\tilde{R}_\delta}(\tilde{u}_3''''-2(\alpha^{\mathrm{t}})^2\tilde{u}_3''+(\alpha^{\mathrm{t}})^4\tilde{u}_3), \tag{46}$$

where $\tilde{R}_\delta = R_\delta\cos\theta$. Equation (46) is just the OS equation governing the stability of a 2D wave mode of wavenumber α^{t} riding on the original mean flow field $U(x_3)$ at the reduced Reynolds number of $\tilde{R}_\delta$. The change in the velocity reference scale to $V_\infty^{(\mathrm{d})}$ has important consequences for the wall properties. The non-dimensionalized properties of the wall given by (44) and (45) now become

$$\tilde{C}_{\mathrm{t}} = C_{\mathrm{t}}(\cos\theta)^{-1}, \quad \tilde{d} = d(\cos\theta)^{-1}, \quad \tilde{G} = G(\cos\theta)^{-2}, \quad \tilde{K} = K(\cos\theta)^{-2}. \tag{47a–d}$$

Rescaling therefore has the effect of making the wall stiffer by increasing the stifness moduli such as G and K by a factor of $(\cos\theta)^{-2}$. Since changing reference scales does not actually affect the physical essence of the problem, the above shows that the stability problem associated with the propagation of an oblique disturbance wave mode $\exp[\mathrm{i}(\alpha x_1+\beta x_2-\omega t)]$ in the basic velocity field $U(x_3)$ at a given Reynolds number R_δ is formally equivalent to the stability problem of the 2D mode $\exp[\mathrm{i}\alpha^{\mathrm{t}}(x_1-ct)]$ perturbing the same velocity field over a stiffer compliant wall at the lower Reynolds number of $\tilde{R}_\delta$. We refer to the increase in stiffness as the *stiffness rescaling* effect and the rescaled problem represented by (46) and (47) as the *rescaled equivalent* 2D problem. The reduction to the rescaled equivalent 2D problem allows known 2D results and trends to be brought to bear on the 3D case.

The stability problem for 2D wave modes ($\beta = 0$) is obviously identical to its rescaled equivalent 2D problem, since $\theta = 0°$ then. When θ is increased from zero to a finite value (that is, going from a 2D to an oblique mode) at a fixed R_δ, the rescaled equivalent 2D problem has a decrease in its $\tilde{R}_\delta$ and an increase in the stiffness of its wall. Reduction in the Reynolds number may generally be regarded as having a favourable influence on stability. The effect of increased wall stiffness on stability, however, depends on the specific class of instability in question. For TS instability, it is well known that its 2D modes are destabilized by an increase in wall stiffness. With such opposing influences acting on the stability of the rescaled equivalent 2D modes, it is difficult to ascertain without detailed calculation whether 3D TSI wave modes are likely to be more dominant than 2D TSI modes at the same R_δ. The relative dominance would undoubtedly depend on the compliant nature of the wall. The compliance-induced instabilities (the CIFI, also termed FISI in works by Carpenter), on the other hand, are suppressed by an increase in wall stiffness. It is recalled here that the travelling wave flutter (TWF) and the static divergence (SD) instabilities are important members of this class. Since both factors tend to favour its stability, the worst case instability for CIFI is most likely to be presented by 2D wave modes. Hence, if the 2D CIFI modes of an unstable branch can be effectively

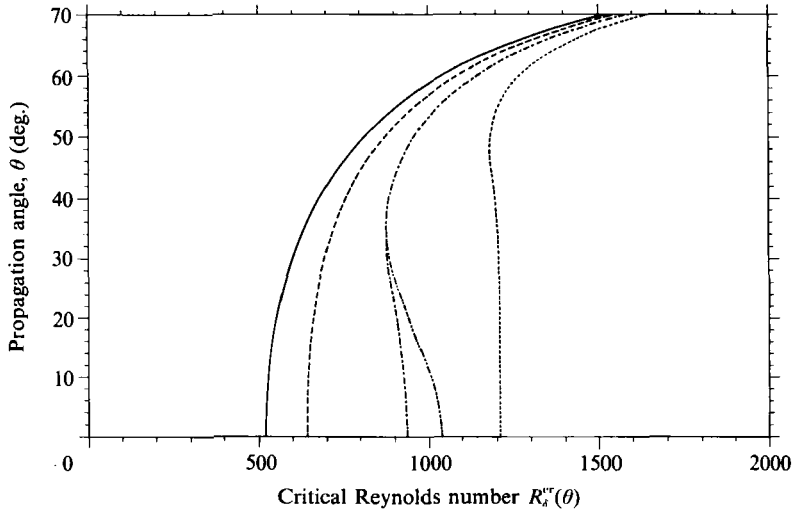

FIGURE 2. Variation of the θ-critical Reynolds number $R_\delta^{cr}(\theta)$ with the propagation angle θ for the TSI regime of some single-layer isotropic-material walls. $h = 1.0$: – – – –, $C_t = 1.0$; – · – · – ·, $C_t = 0.7$; . . . . . , $C_t = 0.5$. · · – · · – · · –, $h = 5.0$, $C_t = 0.7$; ——, rigid wall. In all compliant cases, $d = 0.0049$ and $K = 500$.

suppressed, there should be no 3D CIFI modes of the same branch at the same R_δ. If the purpose is to eliminate the CIFI, two-dimensional study would generally be adequate. For this reason, attention is given below mainly to the consideration of the more complicated case of 3D TSI rather than to 3D CIFI.

3.3. *Critical Reynolds number*

We begin our study of 3D TSI wave modes over isotropic material walls by considering the effects wall compliance has on the critical Reynolds number of the TSI regime. The critical Reynolds number is denoted by R_δ^{cr} and is the value below which no linearly unstable TS modes exist. We introduce the additional notation $R_\delta^{cr}(\theta)$, the θ-critical Reynolds number, to denote the critical Reynolds number taken over the subclass of TSI modes which have propagation angle $\theta = \tan^{-1}(\beta/\alpha)$. Clearly $R_\delta^{cr}(\theta) \geqslant R_\delta^{cr}$. Note that $R_\delta^{cr}(\theta)$ is directly related to the critical Reynolds number of the rescaled equivalent 2D case, denoted by $\tilde{R}_\delta^{cr}(\theta)$, by $\tilde{R}_\delta^{cr}(\theta) = R_\delta^{cr}(\theta)\cos\theta$.

Figure 2 shows the variation of the θ-critical Reynolds number for a number of single-layer compliant walls; the curve for a rigid wall is also shown for comparison. The critical Reynolds number for 2D modes $R_\delta^{cr}(0°)$ on a rigid wall has the value of 519.06. Since the stiffness of a rigid wall is unaffected by the scaling factor $(\cos\theta)^{-2}$, $\tilde{R}_\delta^{cr}(\theta)$ for a rigid wall has the constant value of 519.06, irrespective of the value of θ, and the curve is hence simply given by $R_\delta^{cr}(\theta) = 519.06(\cos\theta)^{-1}$. The critical Reynolds number R_δ^{cr} for the 3D TSI regime on a rigid wall is therefore equal to 519.06 and belongs to a 2D eigenmode ($\theta = 0°$). The effects of wall compliance on the $R_\delta^{cr}(\theta)$-curve and the critical Reynolds number R_δ^{cr} can also be seen in figure 2. Since wall compliance favours the stability of TS modes, the $R_\delta^{cr}(\theta)$-curves for all the compliant walls are found to lie to the right of the rigid-wall curve. For the compliant wall with thickness $h = 1.0$ and elastic shear wave speed $C_t = 1.0$, the R_δ^{cr} also belongs to a 2D mode. For the softer walls ($h = 1.0$) with $C_t = 0.7$ and 0.5, however, the R_δ^{cr} can be seen to be given by oblique wave modes. At $C_t = 0.7$ for example, R_δ^{cr} is approximately 873 and belongs to a mode with $\theta \approx 34°$, compared with $R_\delta^{cr}(\theta) \approx 935$

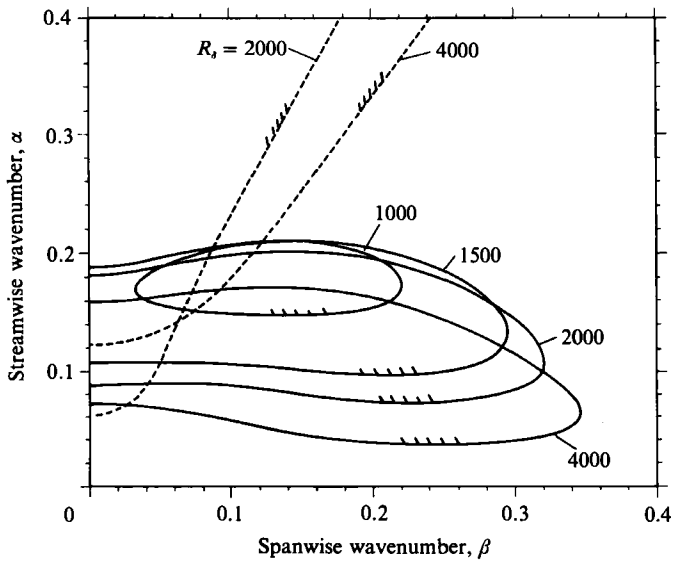

FIGURE 3. α–β sections of the neutral stability surfaces for a single-layer isotropic material wall with $h = 5.0$, $C_t = 0.7$, $d = 0.0049$ and $K = 500$. ——, TSI; – – – –, CIFI. Partial hatching denotes unstable side of neutral curve.

for 2D modes. As the propagation angle θ becomes large, all the $R_\delta^{cr}(\theta)$ curves approach the rigid-wall curve asymptotically. This has a simple explanation. When θ is large (approaching to 90°), the scaling factor $(\cos\theta)^{-2}$ is very large, so that the walls of the rescaled equivalent 2D cases become very stiff and their associated $\tilde{R}_\delta^{cr}(\theta)$ approach the rigid-wall value of 519.06. The $R_\delta^{cr}(\theta)$-curves consequently tend towards the rigid-wall curve of $519.06(\cos\theta)^{-1}$ as θ becomes large. The $R_\delta^{cr}(\theta)$-curve for a thick compliant layer with $h = 5.0$ ($C_t = 0.7$) is also given in figure 2 for comparison with the case with $h = 1.0$. Increase in layer thickness makes the wall more compliant. According to 2D studies, such as Yeo (1988), this will raise the 2D critical Reynolds number, as reflected in the results shown in figure 2. The curves for the two thicknesses, however, converge rapidly as the propagation angle θ becomes moderately large (about 35°). This behaviour can be explained with reference to the 2D results of Yeo (1988). As θ increases, the accompanying increase in the stiffness of the wall of the rescaled equivalent 2D case makes it increasingly difficult for the disturbance waves to penetrate the walls to great depths; see §4.2 of Yeo (1988). The full depth of the thick compliant layer ($h = 5.0$) is therefore not perceived by the 2D modes of the rescaled problem, and consequently also not perceived by their associated 3D modes at large θ. The close identity of the two curves for $\theta > 35°$ indicates that the disturbances associated with those eigenmodes of the thick layer with $\theta > 35°$ probably penetrate the wall to a depth of less than 1.0.

3.4. *The α–β sections of neutral stability surfaces*

Figure 3 shows the α–β sections of the neutral stability surface for the thicker compliant-layer wall ($h = 5.0, C_t = 0.7$) at various R_δ. Partial hatching marks the side of the neutral curves that corresponds to unstable modes. It can be seen that there are no unstable 2D TSI modes at $R_\delta = 1000$. This is consistent with $R_\delta^{cr}(0)$ being greater than 1000 for the wall, see figure 2. At the other R_δ, the α-width of the TSI domains increases as we go from 2D to 3D modes ($\beta \neq 0$). This indicates that the

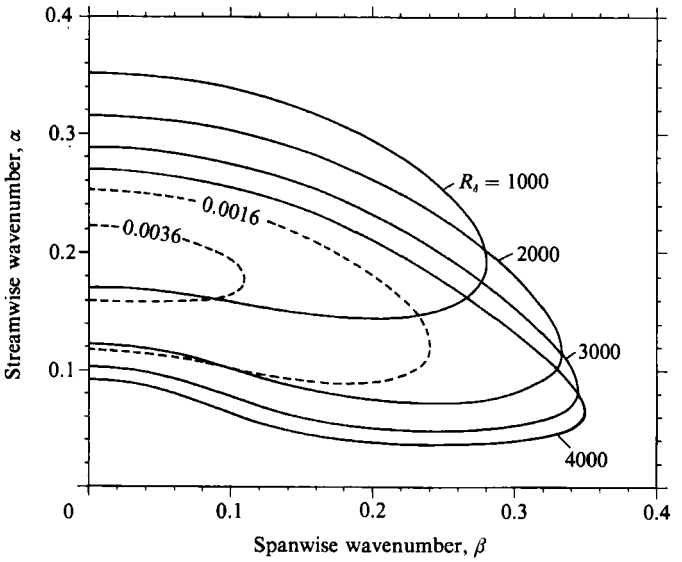

FIGURE 4. α–β sections of the neutral stability surface for a rigid wall. ——, ω_i-contours at $R_\delta = 4000$.

most unstable or dominant modes are most probably 3D. This was indeed confirmed by actual calculations of the temporal growth rates for both 2D and 3D modes. Such results are quite typical of walls with a significant or high degree of compliance; say $C_t < 0.8$ and h many times the displacement thickness of the boundary layer. To avoid crowding figure 3, details on growth rates have not been included. Growth-rate data are given for other compliant walls in later figures. The α–β sections of a rigid wall are given in figure 4. By comparing figures 3 and 4, it is easy to see that the compliant wall in question has much smaller TSI domains at corresponding R_δ. As may then be expected, the compliant wall has temporal and spatial growth rates which are significantly less than those of the rigid wall at corresponding R_δ. Next we note that the maximum propagation angles (largest β/α ratios) for the TSI modes of the compliant wall at $R_\delta = 2000$ and 4000 are approximately 74.5° and 82.4° respectively, very close to the respective values of 74.96° and 82.54° for the rigid wall. This again is a consequence of the stiffness rescaling effect which makes the wall appear very stiff to oblique waves propagating at large θ.

The neutral α–β of sections of the CIFI regime of the compliant wall taken at $R_\delta = 2000$ and 4000 are also displayed in figure 3. These are travelling-wave flutter (TWF) instabilities. The static divergence (SD) instabilities are of no consequence here, being important only in very soft walls with high damping (see Yeo 1990). The maximum propagation angles θ for unstable modes at the two Reynolds numbers of 2000 and 4000 are respectively less than 24° and 31°. The reduction in the disturbance growth rates with increase in θ is fairly rapid. The compliant layer has a lowest free surface wave speed of $c_R \approx 0.9553 C_t$. The wall of the rescaled equivalent 2D case therefore has

$$\tilde{c}_R \approx 0.9553 C_t (\cos\theta)^{-1}.$$

Since the 2D CIFI are known to be well suppressed when the lowest free-surface wave speed of the wall is greater than the free-stream velocity (Yeo 1988), this means that the rescaled 2D case will have no CIFI when $\tilde{c}_R > 1.0$. The consequence of this is that there should be no oblique CIFI modes with propagation angle $\theta > 48°$.

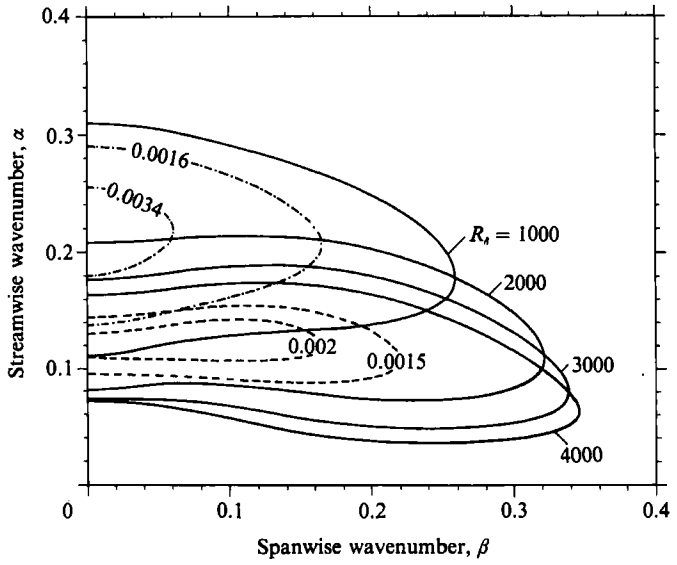

FIGURE 5. α–β sections of the neutral stability surface for the TSI regime of a single-layer isotropic material wall with $h = 5.0$, $C_t = 0.7$, $d = 0.0588$ and $K = 500$. ω_i-contours: ·—·—·—·, $R_\delta = 1000$; – – – –, $R_\delta = 4000$.

3.5. *Effects of wall damping*

We next examine the effects of material damping on the relative dominance of 2D and 3D instability modes. Figure 5 shows the α–β sections for the thick compliant layer of figure 3 when the damping coefficient is increased more than ten times to $d = 0.0588$. The strong CIFI which were present at $d = 0.0049$ (figure 3) are effectively suppressed at this relatively high level of material damping. In fact, the 2D CIFI are well suppressed at $d = 0.0588$ according to figure 13 of Yeo (1988). We therefore do not really expect to find oblique CIFI modes of any consequence.

Damping, in general, has a destabilizing influence on the TSI. Its relative influence on the 2D and 3D instability modes can be seen by comparing figures 3 and 5. We shall examine the lower Reynolds number case first. At $R_\delta = 1000$, the increase in damping introduces 2D TSI modes which were absent at $d = 0.0049$. It is evident from the temporal amplification contours shown that the high level of damping has in fact made the 2D modes more dominant than the 3D modes at $R_\delta = 1000$. Moreover, calculation also indicates that R_δ^{cr} now belongs to a 2D mode. In general, material damping has been found to have a stronger destabilizing effect on 2D TSI compared to 3D TSI. Part of the cause of this can be found by noting that for the rescaled equivalent 2D case, the damping coefficient $\tilde{d}$ of the material scales according to the factor $(\cos\theta)^{-1}$. The relaxation time constant $\tilde{\tau} = \tilde{d}/\rho\tilde{C}_t^2$ of the material then scales as $\cos\theta$. The relaxation time constant is a commonly used measure of the quality of damping. (For example, for the Voigt damping model, the relaxation time constant τ is the time it takes for the strain to attain $(1-e^{-1})$ of the value of the steady-state strain in a standard creep test.) As we increase θ, the rescaled equivalent wall becomes qualitatively less damped. Moreover, when the damping coefficient d is increased, the rescaled equivalent 2D modes also experience a smaller absolute increase in the relaxation time of the material, proportional to $\cos\theta$. If the increase in τ is say 1 s for 2D modes, then the increase in τ for the rescaled 2D equivalent of an oblique wave propagating at $\theta = 60°$ would be 0.5 s. This

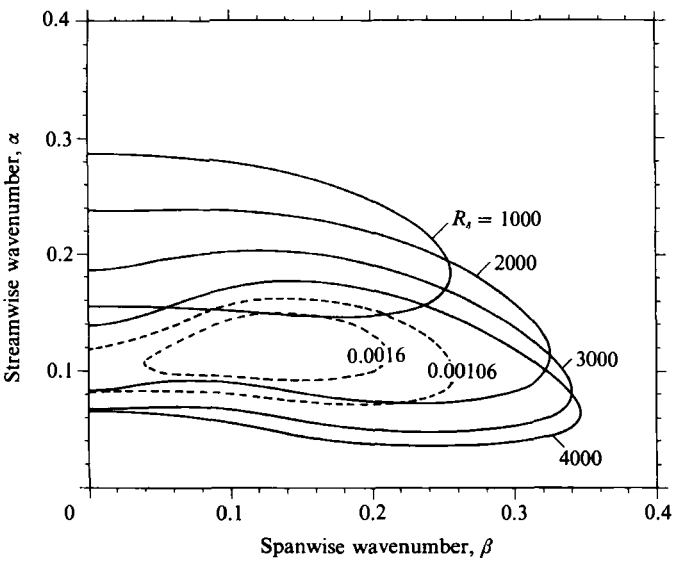

FIGURE 6. α–β sections of the neutral stability surface for the TSI regime of a four-layer isotropic material wall. ------, ω_i-contours at $R_\delta = 4000$. Compliant wall data:

Layer no.	h	C_t	d	K
1	0.5	1.0	0.0049	500
2	1.5	0.8	0.0049	500
3	1.0	0.4	0.0294	0.267
4	0.5	0.8	0.0049	500

qualitatively explains the smaller destabilizing influence of material damping on 3D TSI modes. The perceived stiffness of the wall, as governed by the value of $\tilde{C}_t$ or $\tilde{G}$, also has an important bearing on the effects of wall damping. As θ becomes large, the rescaled wall becomes very stiff. For a very stiff wall, damping can only have a minimal effect on stability because the wall can hardly respond to perturbations. Thus the effects of any changes in damping will be small for oblique TSI with large propagation angle.

For higher R_δ, the difference in the damping level of the two walls produces smaller differences in their respective α–β sections. At $R_\delta = 4000$, these sections of the two walls are almost identical, implying that the amplification rates of the TSI modes are nearly the same for both walls at this Reynolds number. This is consistent with the behaviour noted in Yeo (1988) that material damping has only a small destabilizing effect on the TSI modes at high Reynolds numbers. This in its turn is related to the fact that the TSI modes at high R_δ generally have low frequency. The scaling effect of θ on the relaxation time constant and on the wall stiffness of the rescaled equivalent problem also plays a role in lessening the effect of any difference in damping level on the 3D modes. The consequence of this indifference to material damping is that the 3D TSI modes may remain dominant over the 2D modes even at high levels of damping when the R_δ is large. This is reflected in the α–β section for $R_\delta = 4000$ in figure 5.

3.6. *Transition to turbulence*

We next consider a wall which has shown considerable promise for delaying transition to turbulence according to the 2D study of Yeo (1988, §5.3). This is a four-layer compliant wall, which bears some geometric similarity to the original walls of

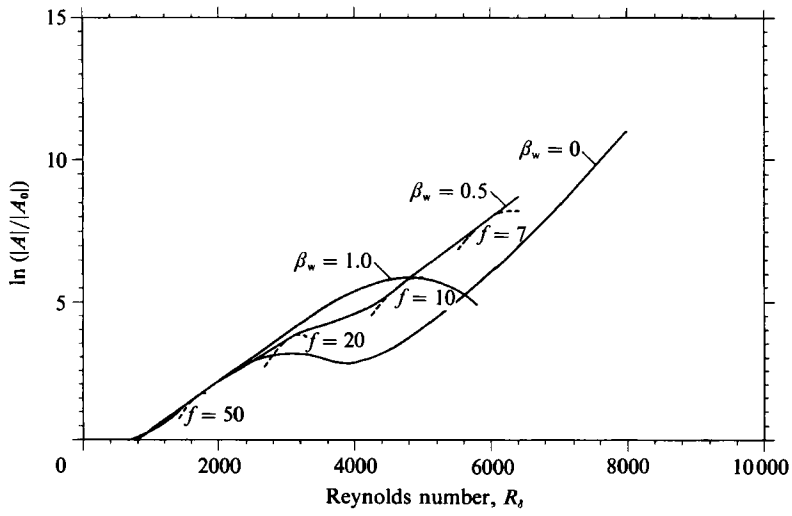

FIGURE 7. The maximum amplification envelopes for the four-layer wall of figure 6 for TSI waves with spanwise wavenumber $\beta_w = 0$, 0.5 and 1.0. ——, Maximum amplification envelope; – – – –, total amplification curve at frequency $F = f \times 10^{-6}$.

Kramer (1960). The important 2D CIFI for this wall are well suppressed; in particular, 2D static divergence is unlikely to be a problem according to the results given in Yeo (1990). The wall has a transition Reynolds number

$$R_x^{tr} \approx 16.27 \times 10^6 (R_\delta \approx 6940)$$

based on the well-known e^n-criterion (n taken to be 8.3) applied to the maximum growth factor for 2D TSI wave modes. The corresponding value for a rigid wall is $R_x^{tr} \approx 2.84 \times 10^6 (R_\delta \approx 2900)$, giving a ratio of transition distances equal to 5.73. Because of the absence of 2D CIFI, we do not expect to find 3D CIFI of any consequence. Figure 6 shows the α–β sections of the TSI regime of the four-layer wall; the thicknesses and material properties of the layers are given in the caption to the figure. Some contours of temporal growth rates ω_i are also given for $R_\delta = 4000$. It is observed that the 3D TSI modes become more and more dominant over the 2D modes as we get to higher R_δ. At $R_\delta = 4000$, the α-width of the TSI regime grows rapidly as we go from 2D to increasingly oblique 3D modes. The fastest growing temporal mode at $R_\delta = 4000$ has growth rate $\omega_i \approx 0.0017$ and propagates at an oblique angle of $\theta \approx 45°$. A rigid wall, on the other hand, has a maximum ω_i at $R_\delta = 4000$ of approximately 0.0042, which belongs to a 2D wave mode. The dominance of the 3D modes over the 2D ones in the range of higher R_δ suggests that a calculation of maximum disturbance growth factor based solely on 2D wave modes is likely to underestimate the true growth potential of a general disturbance, comprising both 2D and 3D wave modes. For the four-layer wall, this is confirmed in figure 7, which shows the maximum amplification factor envelopes for 2D wave modes and selected classes of oblique wave modes. The growing oblique wave modes are assumed to have fixed dimensional wavenumber $\beta^{(d)} = \beta_w (L_w^{(d)})^{-1}$ (recall that $L_w^{(d)}$ is the fixed wall lengthscale). The envelopes are determined from the total (integrated) amplification curves of fixed-β_w downstream-growing spatial wave modes driven at fixed values of the frequency $F = \omega/R_\delta = \omega^{(d)} \nu^{(d)} / (U_\infty^{(d)})^2$. The maximum growth factor (given by the envelope) of $e^{8.3}$ is reached by the oblique modes with $\beta_w = 0.5$ at

$$R_\delta \approx 5900 \ (R_x \approx 11.76 \times 10^6).$$

This is about 1000 less than the value of $R_\delta \approx 6940$ for the 2D modes. For the oblique wave modes with $\beta_w = 1.0$, the maximum growth factor only manages to reach about e^6 at $R_\delta \approx 4700$, followed by the decay of the disturbance modes thereafter. The streamwise Reynolds number $R_x \approx 11.76 \times 10^6$ required by the oblique modes with $\beta_w = 0.5$ to reach the growth factor of $e^{8.3}$ can be regarded as giving an estimate of the kind of transition distance that we may expect to see on the four-layer wall (the actual transition Reynolds number will of course be less than this figure). It represents a substantial reduction from the 2D value of 16.27×10^6, but it is still considerably larger than the value of 2.84×10^6 for a rigid wall. This result highlights the fact that predictions based on 2D modes may substantially overestimate the transition distances on soft compliant walls. However, for many compliant walls, such as the four-layer wall examined here, the potential for lengthy delay of transition still exists in considerable force (by the same $e^{8.3}$-criterion) even when the growth of 3D modes is taken into account. For the four-layer wall, this is not at all surprising because the disturbance growth rates for its 3D modes are so much lower than those for a rigid wall; at $R_\delta = 4000$ for example, the maximum temporal and spatial growth rates for the wall are $\omega_i \approx 0.0017$ and $-\alpha_i \approx 0.006$ (real β) respectively compared with the corresponding figures of 0.0042 and 0.0125 for a rigid wall.

Some comments on the use of downstream-growing spatial modes (real spanwise wavenumber) are now in order. A possible objection to the use of such modes in estimating transition location is that they may not yield the worst-case growth. In fact, such modes would appear to be more appropriate to situations in which the disturbance is produced by a long vibrating ribbon, set at an angle to the free stream, or normal to the free stream with induced spanwise periodicity (corresponding to a symmetric pair of oblique waves). The disturbances responsible for natural transition tend to be much less regular. For disturbances of general form, methods based on wave packet considerations have generally been regarded as more suitable for the determination of worst-case growth, being used for correlation with experiments and transition prediction. The approaches of Cebeci & Stewartson (1980) and Nayfeh (1980) are based on asymptotic wave packet analysis. To find the maximum growth by these methods, one has to follow the growth of the waves (say of fixed frequency) along their paths of growth defined by the ray condition that $\tan\phi = -\partial\alpha/\partial\beta$ be real, where ϕ is the angle the group velocity vector makes with the stream direction. The downstream disturbance growth rate is given by $-(\alpha_i + \beta_i \tan\phi)$ and the maximum is selected if more than one ray is indicated for a given wave. For correlation or prediction of natural transition, maximization of disturbance growth with respect to frequency will also be necessary. The numerical implementation of the full scheme, briefly described in Cebeci & Stewartson, is highly complex and expensive. For 3D flow fields, such as a rotating disk boundary layer, the full approach may be imperative. For strongly unidirectional flow such as the Blasius boundary layer at large R_δ, disturbance growth tends to be predominantly in the downstream direction. This is certainly the case for rigid walls. For plate-type compliant walls, Joslin *et al.* (1991) employed a version of the wave-packet scheme. They found that the group velocity angle ϕ is very small except near the lower TS branch where the growth rates are themselves also small. This indicates that the disturbance growth is mainly in the downstream direction. In fact, after due study, they chose to consider only downstream-growing ($\beta_i = 0$) modes, as we did above, in their e^n-calculations; the main difference lies in their maximization of $-\alpha_i$. On the whole their results lend support to our use of downstream-growing modes to provide a qualitative assessment of the relative importance of 2D versus 3D instabilities in determining transition. It

is thus believed that the major conclusions we have reached above (and in Yeo 1986) concerning the reduction in transition delay from that based on 2D calculations, and the potential of compliant walls to significantly delay transition relative to a rigid wall, are essentially correct. Joslin *et al.* arrived at similar conclusions.

4. Anisotropic-material compliant walls

The fully three-dimensional theory of §2 is applied to two anisotropic-material walls in this section. The first set of results concerns a two-layer wall comprising a thin layer of stiff isotropic material on a thick layer of transversely isotropic material (as in figure 1). The two-dimensional stability of Blasius boundary-layer flow over such walls has been studied in detail by Yeo (1990). Here we are interested in the three-dimensional aspects of flow stability and its consequence for the delay of transition. The second set of results pertains to a single-layer orthotropic material wall. The orthotropy model admits materials which possess different shear moduli in the different planes of its orthogonal frame. This feature of the orthotropy model is exploited here to create a wall which has reduced shear stiffness in the plane transverse to the mean-flow direction. The orthotropic wall is found to have significantly improved 3D Tollmien–Schlichting stability over the corresponding isotropic case. The stress–strain laws for the transverse isotropy and orthotropy models have been presented in §2.5 in their respective material-property frames.

4.1. *A transversely isotropic-material wall*

Since our interest concerns the type of wall studied by Yeo (1990), we shall adopt the assumptions and specifications for material properties employed there. These are briefly described below before we go on to the stability results. Of the five material moduli – shear moduli G and G', Poisson's ratios ν and ν' and Young modulus E' (see §2.5.2) which govern the stress–strain behaviour of transversely isotropic material – we assume for simplicity that

$$G = G' \quad \text{and} \quad \nu = \nu'. \tag{48}$$

We further expressed the shear modulus G in terms of an elastic shear wave speed C_t and a damping coefficient d as

$$G = \rho C_t^2 - \mathrm{i}\omega d, \tag{49}$$

as for the isotropic case. The Poisson's ratio is given in terms of G and a modulus K by

$$\nu = \frac{3K-2G}{2(3K+G)}. \tag{50}$$

Material composites which are derived by embedding a parallel family of straight fibres of a stiff material in a soft isotropic matrix form an important class of transversely isotropic materials. The assumption that $G = G'$ and equation (50) for ν are appropriate when the fibre material constitutes a very small fraction of the total volume of the material. C_t and K can then be interpreted as being given by the elastic shear wave speed and the bulk modulus of the isotropic matrix. The assumption that $\nu = \nu'$ confers a significant degree of compressibility to the material. The Young's modulus along the axis of isotropy (or fibre direction) E' is assigned the complex form of

$$E' = E_f + \mathrm{i}(E)_1,$$

where $E = 2G(1+\nu)$ and E_f is the *elastic* part of E'. The imaginary part of E, $(E)_1$, is introduced to impart damping to uniaxial extension/compression along the axis of isotropy, of an amount equal to that the material would experience if it were isotropic. The material in fact becomes isotropic (with Young's modulus E) if we set

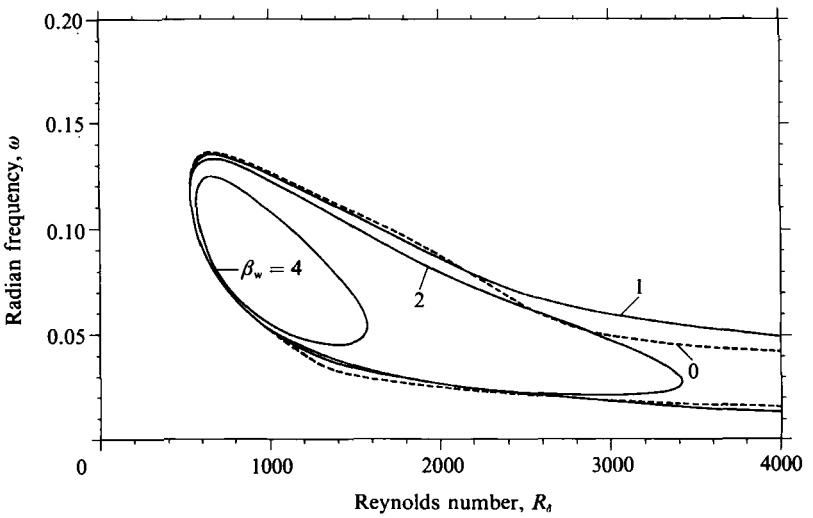

FIGURE 8. The neutral stability curves of the TSI regime at various spanwise wavenumbers β_w for a two-layer anisotropic wall. Layer 1: isotropic material, $h = 0.25$, $C_t = 3.0$, $d = 0.0049$, $K = 1200$. Layer 2: transversely isotropic material with axis of isotropy in the (x_1, x_3)-plane, $h = 4.75$, $C_t = 0.5$, $d = 0.0392$, $K = 500$, $E_f = 30.0$, $A_f = -75°$.

E_f equal to the real part of E so that $E' \equiv E$. The material properties of the transversely isotropic material considered here are therefore specified by the four real parameters

$$C_t, \quad d, \quad K, \quad E_f$$

($\rho = \rho_f$), only one more than for isotropic material. They are assumed to have been non-dimensionalized as in (45) for isotropic materials. The reader will have noted that the above specification for material properties has been designed to provide a natural consistency with the specification for isotropic materials. The interested reader is referred to Yeo (1990) for further details.

Physically, the behaviour of a transversely isotropic material in shear is determined by the shear moduli G and G'. With $G = G'$, the material behaves isotropically in shear. The extension/compression of the material along the fibre axis is governed by the Young's modulus E'. A large value for E_f (real part of E') makes the material very stiff to extension/compression along the fibre axis. In fact, Yeo (1990) was concerned with the study of a class of compliant walls which exhibit strong resistance to extension/compression along a given direction (the fibre axis). The fibre axis was inclined (within the (x_1, x_3)-plane of the wall) at an angle to the direction of the flow; see figure 1. The strong resistance to stretching along the fibre axis (high E_f) was designed to induce disturbance Reynolds stress $-\overline{u_1 u_3}$ of predeterminable sign in the flow as a means to influence the 2D stability of the flow. Here we are interested in the 3D aspects of flow stability for a typical two-layer case which shows potential for delaying transition.

The two-layer wall of interest comprises a thin layer of stiff isotropic material attached onto a much thicker layer of transversely isotropic material with fibre axis inclined at angle $A_f = -75°$, see figure 1. The large value of $E_f = 30$ strongly resists the displacement of the surface along the direction of the fibre axis. The 2D and 3D CIFI (the TWF and SD) for this wall are well suppressed. Figure 8 shows the neutral curves for the two-layer wall for 2D TS wave modes ($\beta_w = 0$) and 3D TS modes of fixed spanwise wavenumber $\beta_w = 1.0$, 2.0 and 4.0. The detailed properties of the wall layers are given in the caption to the figure. It can be seen that the unstable wave

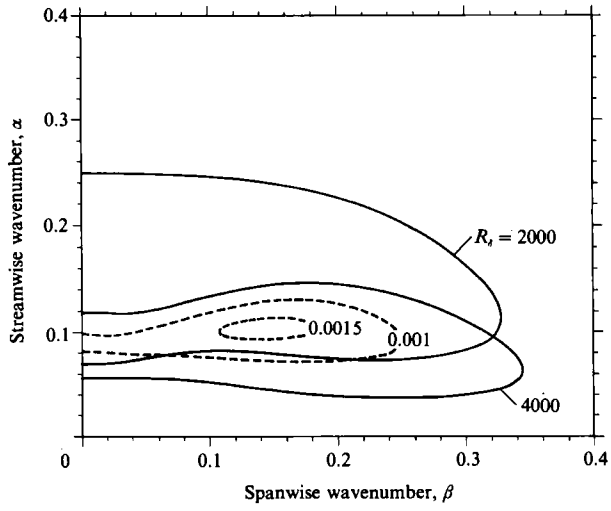

FIGURE 9. α–β sections of the neutral stability surface of the TSI regime for the two-layer anisotropic-material wall of figure 8. – – – –, ω_i-contours at $R_\delta = 4000$.

modes with $\beta_w = 2.0$ and 4.0 have a fairly limited Reynolds-number range. Such oblique modes are therefore not expected to grow to the same extent in the downstream direction as say the unstable modes with $\beta_w = 1.0$. Figure 9 shows the α–β sections of the neutral TS stability surface for the same wall at $R_\delta = 2000$ and 4000. Temporal growth rate contours are also shown for $R_\delta = 4000$. The wall is highly compliant. Overall, the growth rates are very much less than those of a rigid wall (see figure 4). From figure 9, we note that the 3D TSI modes are more dominant than the 2D TSI modes at the higher Reynolds numbers, such as $R_\delta = 4000$. We also note that the neutral sections are close to those of the rigid wall for large propagation angle θ, as for the isotropic cases. The maximum amplification envelopes for 2D TSI modes and oblique TSI modes with spanwise wavenumber $\beta_w = 0.5$ and 1.0 are given in figure 10. For R_δ from 2000 to 6000, the $\beta_w = 1.0$ modes in fact register a higher exponential growth factor than the 2D modes. However, the maximum exponential growth factor reached is only about 4.5, significantly less than the 8.3 used as the criterion here for determining the approximate location of transition. The $\beta_w = 0.5$ modes, however, register higher growth than the 2D modes, with their envelope reaching the exponential factor of 8.3 at $R_\delta \approx 7500$ ($R_x^{tr} \approx 19.0 \times 10^6$) compared with $R_\delta \approx 8400$ ($R_x^{tr} \approx 23.8 \times 10^6$) for the 2D envelope. These results reaffirm the earlier (isotropic) finding that calculations based solely on 2D modes tend to overestimate the actual transition Reynolds numbers (distances). The transition Reynolds numbers obtained by Yeo (1990) are hence on the optimistic side. However, all is not lost. The wall studied above and those walls which demonstrated good potential for transition delay in Yeo (1990) in fact still possess very considerable potential for delaying transition. This is because the growth rates of their 3D modes are very much less than those on a rigid wall. The inclusion of 3D modes probably results in reductions of 20 to 30% in the streamwise Reynolds numbers R_x^{tr} from their corresponding 2D values. Finally, note also that, in many respects, the 3D stability characteristics of the transversely isotropic-material walls studied above and in Yeo (1990) follow the same basic trends that we have noted for isotropic walls in the last section.

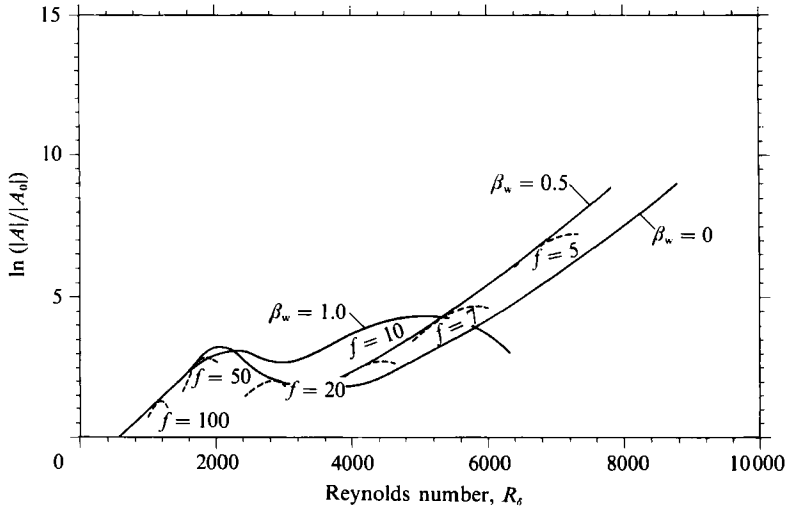

FIGURE 10. The maximum amplification envelope for the two-layer anisotropic wall of figure 8 for TSI waves with spanwise wavenumber $\beta_w = 0$, 0.5, 1.0. ——, Maximum amplification envelope; ------, total amplification curve at frequency $F = f \times 10^{-6}$.

4.2. *An orthotropic-material wall*

The results we have obtained so far, for isotropic-material walls in §3 and transversely isotropic materials in the preceding subsection, demonstrate that 3D oblique TSI modes are generally more dominant than the 2D TSI modes for walls which are sufficiently compliant to admit the possibility of significant transition delay. While significant delay of transition may still be possible in spite of the dominance of the 3D modes (owing to the growth rates being still considerably less than those on a rigid wall), the stability performance of the walls would clearly improve if we can suppress the dominance of the 3D TSI modes relative to the 2D modes. To suppress the higher growth rates of the 3D TSI modes, we need to go back to their cause. The origin of the dominance has been explained in §3.2 in the context of isotropic-material walls, for which the factorization and rescaling of the stability problem permit more direct comparisons to be made between the stability of 2D and 3D modes. To recap, the dominance of the 3D TSI modes is caused by the apparent increase in the wall stiffness which is brought about as a consequence of the reduced velocity field $V(x_3^t)$ on which the oblique waves ride. When the stability problem is rescaled by the reduced free-stream velocity $V_\infty^{(d)}$ to the standard Squire form (46), with the velocity profile $U(x_3^t)$ identical to the 2D case, the wall stiffness moduli are scaled up in value by the factor of $(\cos\theta)^{-2}$. This increase in wall stiffness has a destabilizing influence on the TSI modes and underlies the dominance of the 3D TSI modes, although the effect is ameliorated to some extent by the reduction in the effective Reynolds number. In the case of an isotropic-material wall, the apparent shear modulus perceived by the oblique wave is $G(\cos\theta)^{-2}$, where G is the actual shear modulus of the wall material. To improve the stability of the 3D modes, we need to reduce the value of the perceived wall stiffness, which is governed to a large extent by the value of the rescaled shear modulus $G(\cos\theta)^{-2}$. There is little that one can do about the scaling factor. However, the perceived modulus $G(\cos\theta)^{-2}$ could be reduced if one could reduce the value of G, that is, making G smaller to compensate for the rise in the value of $(\cos\theta)^{-2}$ as θ increases. Therefore a wall which is anisotropic and which possesses reduced material stiffness in oblique directions is required. In this

section, we pursue this idea as a means to reduce the strong dominance of the 3D modes over the 2D modes. Reduced material stiffness in oblique directions is achieved here by employing the appropriate orthotropic-material behaviour.

Let us consider a compliant wall comprising a layer of orthotropic material on a rigid base. First, we assume the material-property frame of the orthotropy model to coincide with the (x_1, x_2, x_3)-coordinate frame of the stability problem. The orthotropic material model is governed by nine independent moduli (see §2.5.1). To keep the model as simple as possible we assume that

$$G_{12} = G_{13} = G, \tag{51a}$$

$$\nu_{12} = \nu_{13} = \nu_{23} = \nu, \tag{51b}$$

$$E_1 = E_2 = E_3 = 2G(1+\nu), \tag{51c}$$

and denote the shear modulus G_{23} in the (x_2, x_3)-plane, which is transverse to the plane of the mean flow, by $G^\perp$. The orthotropic material specified above differs from a completely isotropic material only in that the shear modulus in the transverse plane $G^\perp$ may be different from the shear modulus G in the other two orthogonal planes. If we set $G^\perp = G$, then we would recover an isotropic material with shear modulus G and Poisson's ratio ν. For consistency with the material specification for isotropic-material walls, we express G, $G^\perp$ and ν in terms of elastic shear wave speeds $C_t, C_t^\perp$, damping coefficient d and a bulk modulus K as follows:

$$G = \rho C_t^2 - \mathrm{i}\omega d, \quad G_t^\perp = \rho (C_t^\perp)^2 - \mathrm{i}\omega d, \quad \nu = \frac{3K-2G}{2(3K+G)}. \tag{52a–c}$$

The properties of the orthotropic material are therefore specified by four real parameters: C_t, $C_t^\perp$, d and K, with density $\rho = \rho_f$. The shear stiffness of the material in the transverse (x_2, x_3)-plane is determined by the real part $\rho(C_t^\perp)^2$. We have an isotropic material when $C_t^\perp = C_t$.

While the shear modulus for an isotropic material is well-defined and has the same value for shearing in any plane, it is not always obvious how the shear modulus ought to be defined for an anisotropic material when the plane in question is not one of the principal planes of symmetry. This is because the shear deformation in a non-symmetry plane may be influenced by shear stresses acting in the other planes. Furthermore, the shear stress acting in a non-symmetry plane not only produces shear strain within the plane, but may also simultaneously induces shear strains in the other planes, such as planes transverse to the original plane. Thus for the orthotropic material in question, tensor transformation shows that the shear strain ϵ_{13}^t in the oblique (x_1^t, x_3^t)-plane is in fact related to the in-plane shear stress σ_{31}^t and the transverse-plane shear stress σ_{32}^t as follows:

$$2\epsilon_{13}^t = \left[\frac{G\sin^2\theta + G^\perp\cos^2\theta}{GG^\perp}\right]\sigma_{31}^t + \left[\frac{(G-G^\perp)}{GG^\perp}\sin\theta\cos\theta\right]\sigma_{32}^t. \tag{53}$$

To have some approximate idea how stiff the material is to shearing in the (x_1^t, x_3^t)-plane, we assume a situation in which a sample of the material is subject only to the in-plane shear stress σ_{31}^t; $\sigma_{32}^t \equiv \sigma_{12}^t \equiv 0$. Using (53), we then define the stiffness to (modulus of) shearing as the ratio of applied stress to the resultant strain in the same plane (similar to the conventional definition for shear modulus), that is $\sigma_{31}^t/(2\epsilon_{13}^t)$, and denote this ratio by

$$G^{\mathrm{obl}}(\theta) = \frac{GG^\perp}{G\sin^2\theta + G^\perp\cos^2\theta}. \tag{54}$$

$G^{\mathrm{obl}}(\theta)$ is termed the *oblique shear modulus* here and its magnitude is a measure of the

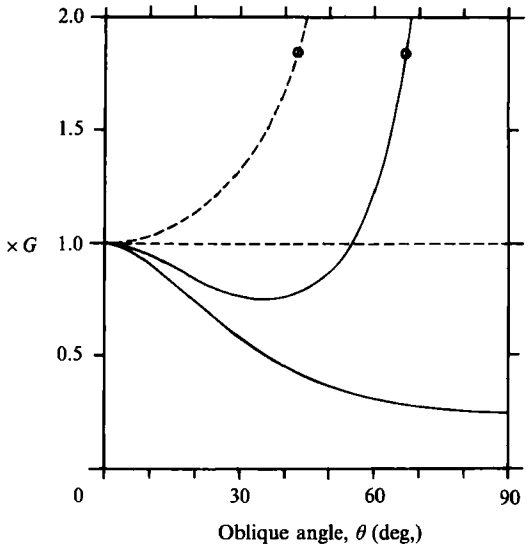

FIGURE 11. Shear moduli in the (x_1^t, x_3^t)-plane. Elastic-orthotropic-material wall with $G^\perp/G = 0.25$: ——, G^{obl}; ⊖——, $G^{\text{obl}}(\cos\theta)^{-2}$. Isotropic-material wall: – – – –, G; ⊖– – –, $G(\cos\theta)^{-2}$.

resistance (stiffness) of the material to shearing in the (x_1^t, x_3^t)-plane when subject to shear stress σ_{31}^t acting in the plane. We note that this is an approximate measure because in an actual problem σ_{32}^t may not be zero and its value may increase or decrease the actual strain produced according to (54). When $\theta = 0°$, $G^{\text{obl}} = G$ and when $\theta = 90°$, $G^{\text{obl}} = G^\perp$ as we would expect. If $G > G^\perp$, which is the case of interest here, $G^{\text{obl}}(\theta)$ is a monotonically decreasing function of θ for θ between 0 and 90°. This affirms our intuitive feeling that if the shear modulus $G^\perp$ in the transverse (x_2, x_3)-plane is made less than the shear modulus G in the (x_1, x_3)-plane of the mean flow, then the 'shear modulus' in the oblique-wave plane (x_1^t, x_3^t) decreases towards $G^\perp$ as the oblique-wave angle θ is increased. Figure 11 shows the variation of G^{obl} with θ for $G^\perp/G = 0.25$ $(G_t^\perp/C_t = 0.5)$ (zero damping assumed), corresponding to the case studied below. G^{obl} decreases monotonically from the value of G to $G^\perp$ as θ varies from 0 to 90°, while the shear modulus remains constant at G for an isotropic material. The rescaled moduli $G^{\text{obl}}(\cos\theta)^{-2}$ for the orthotropic case and $G(\cos\theta)^{-2}$ for the isotropic case are also depicted: that the isotropic case rises monotonically and rapidly as θ is increased, while for the orthotropic case it is actually less than G for θ up to about 55°.

Results are given here for an orthotropic layer of thickness $h = 5.0$ backed by a rigid base. The elastic shear wave speeds C_t and $C_t^\perp$ for the mean-flow and transverse planes are 0.7 and 0.35 respectively. The damping coefficient $d = 0.0098$ and the bulk modulus $K = 500.0$. The ratio $G^\perp/G$ based on the elastic part of the shear moduli is 0.25. Figure 12 shows the neutral α–β sections of the TSI regime for the orthotropic walls at $R_\delta = 2000$ and 4000. Also shown are the corresponding α–β sections for the isotropic case which has $C_t = C_t^\perp = 0.7$. Comparison between the two sets of results is rendered easy here because the selection of properties for the orthotropic material made the orthotropic wall behave exactly like the isotropic wall to 2D ($\beta = 0$) waves and the two walls have identical 2D flow stability characteristics. It is observed that for both Reynolds numbers, the orthotropic-material wall, with its reduced transverse shear stiffness, has unstable TSI regimes which are noticeably narrower than those of the isotropic wall. The narrowing of the α-width occurs mainly on the

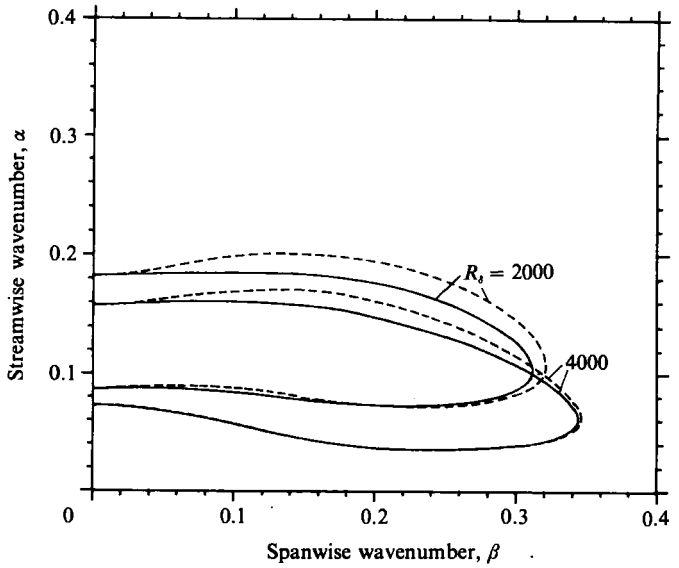

FIGURE 12. α–β sections of the neutral stability surfaces of the TSI regimes for the orthotropic-material and the isotropic-material walls. ——, Orthotropic case with $h = 5.0$, $C_t = 0.7$, $C_t^{\perp} = 0.35$, $d = 0.0098$, $K = 500$; – – – –, isotropic case with $h = 5.0$, $C_t = 0.7$, $d = 0.0098$, $K = 500$.

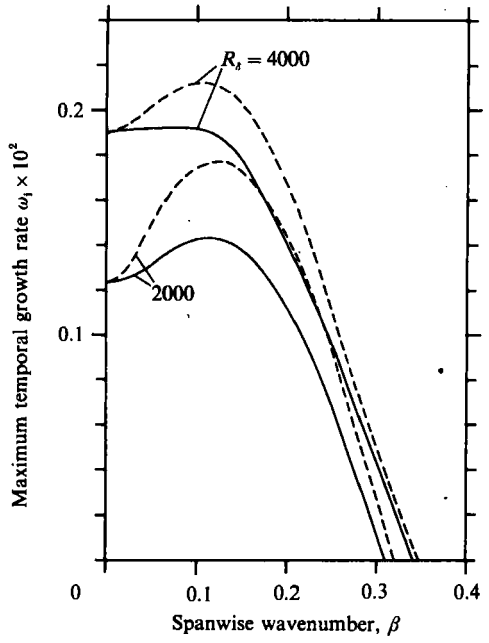

FIGURE 13. The maximum temporal growth rate ω_i as a function of spanwise wavenumber β for the walls of figure 12; maximization with respect to wavenumber α. ——, Orthotropic case; – – – –, isotropic case.

upper branches of the neutral boundaries, while the lower branches are nearly identical for the two walls. The decrease in the size of the unstable regimes shows that both the temporal and downstream spatial growth rates for the orthotropic-material wall are lower than those for the isotropic-material wall. The maximum temporal growth rate ω_i, distributed as a function of the spanwise wavenumber β, for the two

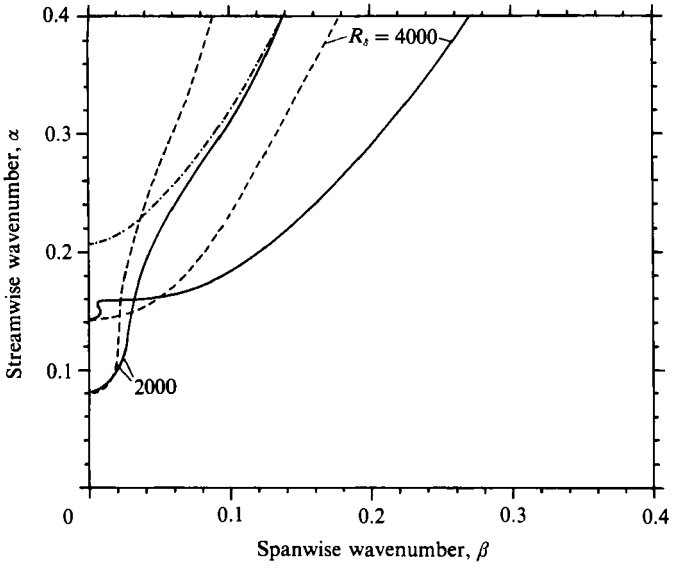

FIGURE 14. α–β sections of the neutral surfaces of the primary CIFI regimes for the orthotropic-material and the isotropic-material walls. ——, Orthotropic case; – – – –, isotropic case; ·–·—·—·–·, orthotropic case with $d = 0.0196$ ($R_\delta = 4000$).

walls are compared in figure 13. For the isotropic case, the strong dominance of the 3D modes over the 2D ones is clearly evident at both the Reynolds numbers of 2000 and 4000. This dominance is seen to be greatly reduced, though not eliminated, in the case of the orthotropic-material wall. At $R_\delta = 4000$, the maximum ω_i for the 3D modes of the orthotropic wall is nearly equal to that for the 2D modes. At even higher Reynolds numbers, the 2D modes may be expected to become the more dominant ones. The reductions in the 3D growth rates from corresponding isotropic values are in fact quite significant. A further small decrease in the transverse shear modulus $G^\perp$ or the elastic shear speed $C_t^\perp$ is sufficient to render the 3D modes less dominant than the 2D ones for Reynolds numbers above 3000.

The improved stability of the 3D TSI modes for the orthotropic-material wall over that of the isotropic-material wall is not without its cost. The decrease in the stiffness of the wall in the oblique-wave planes can destabilize oblique CIFI (both TWF and SD) wave modes, and may even bring into existence new 3D CIFI regimes if the shear stiffness in the oblique planes is reduced sufficiently. This destabilization of the CIFI regimes can be seen in figure 14 which illustrates the neutral α–β sections of the primary CIFI regimes, a TWF, for the two walls. Fortunately, in this and many other cases, the enhanced TWF regimes brought about by reduced transverse wall stiffness can be suppressed by increasing the damping coefficient d of the material. An increase in the value of d from 0.0098 to 0.0196 for the orthotropic-material wall is sufficient to suppress the TWF regime at $R_\delta = 2000$. The same increase greatly reduces the size of (and hence the growth rates in) the TWF regime at $R_\delta = 4000$; see figure 14. A further increase in the value of d to say 0.025 is sufficient to suppress the TWF at $R_\delta = 4000$. SD instability is not expected to be important at the present level of stiffness and damping (see §3.5 of Yeo 1990). With the CIFI under control, the orthotropic case ($C_t^\perp/C_t = 0.5$) with its considerably subdued 3D TSI modes may be expected to perform better than the isotropic case ($C_t^\perp/C_t = 1.0$) in terms of transition delay. Increase in the damping, however, may not have the above desired

effect on the 3D CIFI if $C_t^{\perp}$ is very low. A coalescence-type instability between 3D CIFI (TWF) and TSI modes, similar to that already encountered in the 2D stability study of isotropic-material walls (Yeo 1988), could well set in.

The results presented in this section demonstrate that the adverse effect imposed on the stability of 3D TSI wave modes by the apparent increase in wall stiffness can be greatly ameliorated, if not overcome, by the employment of the appropriate type of material anisotropy.

5. On surface-based models and optimization

5.1. *The three-dimensional stability of surface models*

The absence of unstable vertical vorticity modes and the reducibility of the three-dimensional stability problem to a rescaled equivalent two-dimensional one are properties generic (model-independent) to walls which behave isotropically with respect to all directions in the (x_1, x_2)-plane. Oblique wave modes over isotropic plate and membrane surfaces are therefore subject to the effects of stiffness rescaling and reduction in effective Reynolds number. In the case of isotropic plates, the flexural rigidity perceived by an oblique wave mode is scaled in magnitude by the factor $(\cos\theta)^{-2}$; the same scaling factor also applies for the tension of an isotropic membrane. Recalling the general similarity in the 2D stability behaviour of these surface models and layered walls, we can conclude with reasonable confidence that much of the 3D-related trends that we have elicited for isotropic-material walls in §3 are also applicable to isotropic plate and membrane surfaces. This similarity in 3D stability behaviour has now been confirmed in the recent work of Joslin *et al.* (1991).

Plate and membrane surfaces can also be endowed with anisotropy. A plate with reduced flexural rigidity in the spanwise direction can be achieved through the use of an orthotropic plate model. A membrane with reduced spanwise stiffness can in theory be obtained by reducing the tension in that direction. It is presumably also possible in theory to have an anisotropic spring foundation. The 3D stability behaviour we have noted in §4.2 for an orthotropic viscoelastic layer is broadly expected to hold for these surfaces, although there can certainly be differences in the details.

The expected similarity stems from the realization that in both the 2D and 3D situations, the OS equation (11*a*) holds the key to flow instability, and the VV equation (11*b*) plays only a secondary role and sometimes no role at all. This is because the $\hat{u}_2^t$-fluctuation, governed by the VV equation, is not able to draw energy directly from the basic flow, and relies upon the presence of a co-existing OS mode for its growth. This is readily appreciated when one derives the energy equation governing the $\hat{u}_2^t$-fluctuation from the VV equation or its equivalent. Within the flow domain, the anti-plane velocity component, $\hat{u}_2^t$, governed by the VV equation, cannot influence the course set by the OS equation. In fact, it is the other way round: the $\hat{u}_2^t$-fluctuation is driven by the OS mode. The VV equation can only affect the OS mode via the boundary to the flow domain, that is via the compliant wall, and then this is only possible in the case of anisotropic walls where there is in general a non-trivial coupling between the in-plane and anti-plane components of displacement (see §2.6). For an isotropic wall, where such coupling is absent, the VV equation has absolutely no influence on linear (non-resonant) instability. The inability of the VV equation to extract energy directly from the basic flow underlies the absence, established in §2.6, of temporally growing $\hat{u}_2^t$-eigenmodes for the rigid and isotropic walls. The role of the VV equation may become significant, however, in cases where

the coupling between in-plane and anti-plane wall displacements is strong. But in any case, it is clear from the above that this influence will be secondary to the direct interaction between the anisotropic wall response and the oblique OS equation. For the interaction, which strongly determines the flow stability, the perceived stiffness of the wall in oblique directions is crucial. Since this perceived wall stiffness is a primary determinant of 3D stability behaviour, then obviously all anisotropic walls with the same type of variation of wall stiffness with oblique wave direction will tend to have a similar type of 3D stability behaviour. Thus orthotropic plates and orthotropic material layers may be expected to share common 3D stability features. The same may be said for Grosskreutz-type anisotropic plate surfaces and the layered walls of §4.1.

The 3D stability of boundary-layer flow over Grosskreutz-type anisotropic plates and orthotropic plates with reduced spanwise flexural rigidity was also investigated by Joslin *et al.* (1991). An example featuring zero spanwise flexural rigidity was given. Their results concur with the above expectations.

5.2. *Optimization*

The compliant walls we have studied in §§3 and 4 above are by no means optimal in the sense of promoting transition delay. Optimization of transition delay for the types of wall we have examined, which may be multi-layer and anisotropic, will certainly be a major computational undertaking in view of the large number of wall parameters that may be involved and the cost of computing transition based on an e^n rule. For volume-based models at least, a sound basis for an optimization procedure is still lacking, although a useful procedure had been introduced by Carpenter (1985) for the simpler plate model.

Carpenter (1985) optimized the performance of his plate surfaces by first requiring that they be marginally stable with respect to the TWF and SD, both as hydroelastic (potential flow) instabilities, and then assessing the ability of the walls to stabilize the TSI by examining the growth rates of the TSI at a fixed Reynolds number ($R_\delta = 2240$, corresponding to the location where a rigid wall has maximum TSI growth rate, is frequently used). The use of hydroelastic criteria is on the conservative side as Carpenter acknowledged. In fact, in the viscous case, TWF can easily be kept at bay to large R_δ with wall damping, so long as the wall is not so soft as to admit a TWF–TSI coalescence. SD instabilities tend to be less of a threat in the laminar boundary-layer case (see §3.5 of Yeo 1990). Furthermore, the choice of R_δ is to an extent questionable and needs more careful justification. These inadequacies must, however, be viewed in the context of the difficulty and cost of actually optimizing with respect to a e^n rule, and Carpenter must be credited with having devised a practical scheme which can be employed for the preliminary design of transition-delaying plate surfaces.

Carpenter's scheme, however, is not easily extended to the category of compliant walls studied here. This is because the hydroelastic TWF and SD criteria for the present types of wall are, in general, definable only in a numerically implicit manner, and cannot be given closed algebraic form, except for the simplest case of a single incompressible isotropic layer. For this simplest case, marginal stability with respect to both hydroelastic TWF and SD instabilities yields an elastic shear wave speed of $C_t = 1.0468$ and a density of $\rho = 0.4563$ according to the theory of Yeo & Dowling (1987), with thickness of layer and level of material damping playing no direct role. To extend Carpenter's scheme for hydroelastic stability to multi-layer walls, complicated numerical procedures to implement and also match the two hydroelastic

criteria would have to be resorted to. Carpenter's procedure had been worked out for 2D instabilities. For anisotropic walls, the hydroelastic criteria would have to account for the possibility of dominant 3D TWF and SD instability modes. For optimization with respect to the TSI, the scheme of Carpenter would also need to be refined to take into account the dominance of 3D TSI modes, now that we are aware of their critical importance. It is useful to note that Carpenter (1991) has recently extended his 2D optimization scheme to multiple-panel plate surfaces (panels placed in sequence downstream).

The primary interest of the present paper has been in the physics, rather than the more practical concern of obtaining the largest possible transition delay. The latter is a separate problem, deserving a separate study, and with a level of difficulty dependent on how stringent one chooses to be about achieving optimality. No attempt has been made to optimize the performance of the walls studied in §§3 and 4, although some of them do possess good potential for delaying transition with the CIFI well under control. The better performing walls had been selected based on their good 2D transition delaying potentials (see Yeo 1988, 1990), which, it is pertinent to note, are of similar order to those quoted by Carpenter and coworkers for their optimized plate surfaces. With the great freedom available for the design of solid layered walls, transition delays significantly greater than those on compliant membrane and plate surfaces cannot be ruled out.

6. Concluding summary and remarks

The linear stability of three-dimensional (oblique) disturbance wave modes in quasi-parallel two-dimensional flows over compliant walls possessing general material anisotropy was formulated. Our approach differs significantly from that of Carpenter & Gajjar (1990), and sheds more light on the physics of 3D wave modes. For walls whose material stress–strain behaviour is isotropic with respect to all directions in the (x_1, x_2)-plane, it was shown that the 3D stability eigenvalue problem for unstable normal modes can be reduced to an equivalent 2D one involving the Orr–Sommerfeld equation (11*a*). This reduction is possible because the spectrum associated with the vertical vorticity equation (11*b*) was shown to comprise only damped modes. This reduction cannot be extended to anisotropic material walls in general because the governing equations for wall motion do not decouple as do the flow equations.

The case of isotropic-material walls was studied in detail. The reduction allows many features of 3D flow stability to be explained on the basis of 2D results. Furthermore, a simple rescaling of the equivalent 2D problem reveals that the relative stability of the 2D and 3D wave modes are governed by two factors: namely, the apparent reduction in the Reynolds number of the flow and the apparent increase in the material stiffness of the wall perceived by oblique waves. The first factor tends to favour stability. The effect of the second factor, referred to as the stiffness rescaling effect, depends on the class of instability in question. Increase in wall stiffness favours the stability of the CIFI. The worst-case instability for CIFI is therefore normally presented by 2D modes. To eliminate CIFI, two-dimensional study appears adequate. The TSI are destabilized by increases in wall stiffness. With the two factors in opposition, it is not known *a priori* if 2D or 3D modes are going to be the more dominant ones. Results indicate that the apparent increase in wall stiffness is indeed an important factor and that 3D/oblique TSI modes tend to become more dominant than the 2D modes when the wall is sufficiently compliant.

A consequence of the dominance of the 3D modes is that the critical Reynolds number for the TSI regime of a compliant wall may be given by 3D modes. The faster growth of the 3D modes also implies that the prediction of transition (e^n rule) based solely on 2D modes, the common practice, would overestimate the true transition distance; and that for more realistic estimation, the growth of 3D modes must be considered. The reduction in transition distances from corresponding 2D values may be significant for some highly compliant walls. However, since wall compliance has a stabilizing influence on both 2D and 3D TSI modes, the TSI growth rates on a highly compliant wall may yet be much lower than those on a rigid wall. Thus a highly compliant wall (in the absence of overwhelming CIFI) may yet be able to offer substantial delay of transition over the rigid-wall case. The effects of material damping were also investigated. Material damping tends to have a stronger destabilizing effect on TSI wave modes propagating at smaller oblique angles. Material damping may therefore alter the relative dominance of the 2D and 3D modes. Examples presented show that an increase in material damping can make the critical Reynolds number belong to a 2D mode when it originally belonged to a 3D one. The effects of material damping on the TSI regime, however, diminish rapidly and become quite unimportant at high Reynolds number or when the propagation angle θ is large.

The emphasis above on 3D modes should not be taken to mean that 2D studies are misleading or useless. For isotropic walls at least, 2D stability characteristics generally give a good indication of the ability of the wall to stabilize the TSI modes. For the elimination of CIFI on isotropic walls, 2D studies are usually adequate. 2D studies are particularly useful as a guide to the relative ability of isotropic walls to suppress flow instabilities. They are therefore applicable as a guide to the selection of walls for more careful and expensive 3D scrutiny. An isotropic wall with undesirable 2D stability characteristics could not be expected to perform well in transition delay. In the same vein, estimates of transition distances based on 2D modes could also provide a relative guide to the walls' ability to delay transition, although the predicted transition distances by themselves must be viewed with some suspicion.

A good deal of what we have said above concerning isotropic-material walls is also applicable when the material is anisotropic. This is because the potential for flow instability actually resides with the Orr–Sommerfeld equation (11*a*). The vertical vorticity equation (11*b*) cannot extract energy for the growth of u_2^{ι}-mode from the mean flow except in the presence of a non-zero u_3^{ι} component of disturbance velocity. This is in fact the underlying physical cause for the absence of unstable modes in the spectrum of the VV equation for walls possessing material isotropy in the (x_1, x_2)-plane. For anisotropic-material walls in general, however, there is no distinct VV spectrum because of the non-trivial coupling between the in-plane and anti-plane components of wall motion. The coupling allows the VV equation to exercise some degree of influence on the OS equation. As a consequence of the pre-eminent role of the OS equation, even for the anisotropic cases, the stability of 3D/oblique wave modes on anisotropic walls is also strongly influenced by the scaling effect on wall stiffness and the reduction in effective Reynolds number. Whilst recognizing this similarity with the isotropic case, it should be noted that material anisotropy does offer one important advantage over isotropy in that the effect of stiffness scaling, which is inimical to the stability of the TS modes, could be ameliorated by the choice of anisotropies that have reduced material stiffness in oblique planes. An example featuring such anisotropy was presented. The reduced material stiffness in oblique

planes partially neutralized the stiffness rescaling effect so that the oblique waves perceived a softer wall. This led to a very significant reduction in the growth rates of the 3D modes relative to those of the 2D modes. Such anisotropy may, however, encourage the enhancement or onset of oblique CIFI. In many cases, however, the enhanced CIFI may be suppressed by increasing the material damping. Whenever the anisotropy does not confer reduced material stiffness in oblique directions/planes, the effect of stiffness rescaling generally leads to enhanced growth rates for the 3D TSI wave modes, much as in the isotropic case.

In spite of the essential pre-eminence of the OS equation, the role of the VV equation should not be regarded as being entirely trivial. The coupling between the in-plane and the anti-plane components of displacement that is present within the anisotropic-material walls allows disturbance energy to be exchanged between the fluctuations governed by the OS and the VV equations. A flow of energy from the OS mode to the VV mode (necessarily via the wall) may well help to destabilize the OS mode if the mode is of Class A type, and stabilize the OS mode if it is of Class B type. A flow of energy from VV mode to OS mode may have the reverse effect on stability. This energy effect is worth more careful investigation and may be particularly important for walls which are elastic or mildly damped. It is possible that material anisotropy may provide a means with which the direction of energy flow may be selectively managed to improve flow stability.

The author wishes to thank Dr Ann P. Dowling for the invaluable guidance and encouragement she had given him during the course of this work. The author also benefitted greatly from the various discussions with Professor M. Gaster to whom he would like to register his greatest appreciation herein. A large part of this work was done while the author was on study leave at the University of Cambridge. The financial support of the National University of Singapore and the Commonwealth Trust Fund is gratefully acknowledged.

REFERENCES

BENJAMIN, T. B. 1960 Effects of a flexible boundary on hydrodynamic stability. *J. Fluid Mech.* **9**, 513.

BENJAMIN, T. B. 1963 The three-fold classification of unstable disturbances in flexible surfaces bounding inviscid flows. *J. Fluid Mech.* **16**, 436.

BRIGGS, R. J. 1964 *Electron-stream Interaction with Plasmas.* Monograph 29. MIT Press.

CARPENTER, P. W. 1984 A note on the hydroelastic instability of orthotropic plates. *J. Sound Vib.* **95**, 553.

CARPENTER, P. W. 1985 The optimization of compliant surfaces for transition delay. *University of Exeter, School of Engineering, Tech. Note* 85/2.

CARPENTER, P. W. 1990 Status of transition delay using compliant walls. In *Viscous Drag Reduction in Boundary Layers* (ed. D. M. Bushnell & J. N. Heffner), p. 79. AIAA.

CARPENTER, P. W. 1991 The optimization of multiple-panel compliant walls for delay of laminar-turbulent transition. *AIAA Paper* 91-1772.

CARPENTER, P. W. & GAJJAR, J. S. B. 1990 A general theory for two- and three-dimensional wall-mode instabilities in boundary layers over isotropic and anisotropic compliant walls. *Theor. Comp. Fluid Dyn.* **1**, 349.

CARPENTER, P. W. & GARRAD, A. D. 1985 The hydrodynamic stability of flow over Kramer-type compliant surfaces. Part 1. Tollmien–Schlichting instabilities. *J. Fluid Mech.* **155**, 465.

CARPENTER, P. W. & GARRAD, A. D. 1986 The hydrodynamic stability of flow over Kramer-type compliant surfaces. Part 2. Flow-induced surface instabilities. *J. Fluid Mech.* **170**, 199.

CARPENTER, P. W. & MORRIS, P. J. 1989 Growth of three-dimensional instabilities in flow over

compliant walls. In *Proc. Fourth Asian Congr. Fluid Mech., Hong Kong* (ed. N.W.M. Ko & S.C. Kot), Vol. 2, p. A206.

CARPENTER, P. W. & MORRIS, P. J. 1990 The effects of anisotropic wall compliance on boundary-layer stability and transition. *J. Fluid Mech.* **218**, 171.

CEBECI, T. & STEWARTSON, P. J. 1980 On stability and transition in three-dimensional flows. *AIAA J.* **18**, 398.

CHRISTENSEN, R. M. 1979 *Mechanics of Composite Materials.* John Wiley & Sons.

CRAIK, A. D. D. 1971 Nonlinear resonant instability in boundary layers. *J. Fluid Mech.* **50**, 393.

DAVEY, A. & REID, W. H. 1977 On the stability of stratified viscous plane Couette flow. Part 1. Constant buoyancy frequency. *J. Fluid Mech.* **80**, 509.

DRAZIN, P. G. & REID, W. H. 1981 *Hydrodynamic Stability.* Cambridge University Press.

FUNG, Y. C. 1965 *Foundations of Solid Mechanics.* Prentice-Hall.

GAD-EL-HAK, M., BLACKWELDER, R. F. & RILEY, J. J. 1984 On the interaction of compliant coatings with boundary-layer flows. *J. Fluid Mech.* **140**, 257.

GASTER, M. 1975 A theoretical model of a wave packet in the boundary layer on a flat plate. *Proc. R. Soc. Lond.* A **347**, 271.

GASTER, M. 1987 Is the dolphin a red herring? In *Proc. IUTAM Conf. on Turbulence Management and Relaminarization, Bangalore, India* (ed. H. W. Liepmann & R. Narisimha), p. 285. Springer.

GRAY, J. 1936 Studies in animal locomotion VI: The propulsive power of the dolphin. *J. Exp. Biol.* **13**, 192.

GREEN, A. E. & ZERNA, W. 1968 *Theoretical Elasticity.* Oxford University Press.

GUSTAVSSON, L. H. & HULTGREN, L. S. 1980 A resonant mechanism in plane Couette flow. *J. Fluid Mech.* **98**, 149.

JOSLIN, R. D., MORRIS, P. J. & CARPENTER, P. W. 1991 The role of three-dimensional instabilities in compliant wall boundary layer transition. *AIAA J.* (to appear).

KACHANOV, YU. S. & LEVCHENKO, V. YA. 1984 The resonant interaction of disturbances at laminar-turbulent transition in a boundary layer. *J. Fluid Mech.* **138**, 209.

KAPLAN, R. E. 1964 The stability of laminar boundary layers in the presence of compliant boundaries. Sc.D. thesis, MIT.

KLEBANOFF, P. S., TIDSTROM, K. D. & SARGENT, L. M. 1962 The three-dimensional nature of boundary layer instability. *J. Fluid Mech.* **12**, 1.

KRAMER, M. O. 1960 Boundary layer stabilization by distributed damping. *J. Am. Soc. Naval Engrs* **73**, 25.

LANDAHL, M. T. 1962 On the stability of a laminar incompressible boundary layer over a flexible surface. *J. Fluid Mech.* **13**, 609.

LEKHNITSKII, S. G. 1963 *Theory of Elasticity of an Anisotropic Elastic Body.* Holden-Day.

MACK, L. M. 1978 Three-dimensional effects in boundary-layer stability. In *Proc. 12th Symp. Naval Hydrodynamics*, p. 63. National Academy of Science, Washington.

NAYFEH, A. H. 1980 Stability of three-dimensional boundary layers. *AIAA J.* **18**, 406.

NONWEILER, T. 1963 Qualitative solution of the stability equation for a boundary layer in contact with various forms of flexible surface. *Aero Res. Coun. Rep. CP* 622.

RILEY, J. J., GAD-EL-HAK, M. & METCALFE, R. W. 1988 Compliant coatings. *Ann. Rev. Fluid Mech.* **20**, 393.

SARIC, W. S. & THOMAS, A. S. W. 1984 Experiments on subharmonic route to turbulence in boundary layers. In *Turbulence and Chaotic Phenomena in Fluids, Proc. IUTAM Symp., Kyoto* (ed. T. Tatsumi). North-Holland.

SQUARE, H. B. 1933 On the stability of three-dimensional disturbances of viscous flow between parallel walls. *Proc. R. Soc. Lond.* A **142**, 621.

STUART, J. T. 1963 Hydrodynamic stability. In *Laminar Boundary Layer* (ed. L. Rosenhead), p. 492. Clarendon.

WILLIS, G. J. K. 1986 Hydrodynamic stability of boundary layers over compliant surfaces. Ph.D. thesis, University of Exeter.

YEO, K. S. 1986 The stability of flow over flexible surfaces. Ph.D. thesis, University of Cambridge.

YEO, K. S. 1988 The stability of boundary-layer flow over single- and multi-layer viscoelastic walls. *J. Fluid Mech.* **196**, 359.

YEO, K. S. 1990 The hydrodynamic stability of boundary-layer flow over a class of anisotropic compliant walls. *J. Fluid Mech.* **220**, 125.

YEO, K. S. & DOWLING, A. P. 1987 The stability of inviscid flows over passive compliant walls. *J. Fluid Mech.* **183**, 265.